MASTER'S THESIS IN THEORETICAL PHYSICS

Cellular Oscillations in Models of Biological Tissues

Maria Inês Cravo

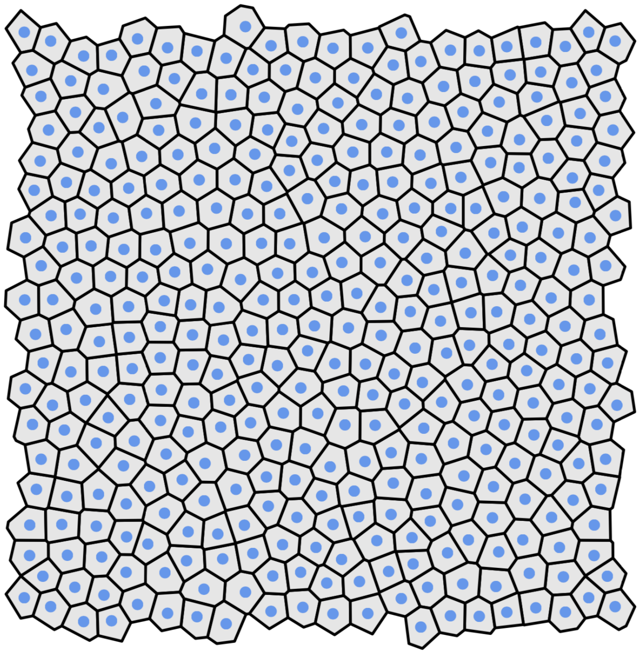

Supervisor: Dr. Joost de Graaf

Institute for Theoretical Physics
Utrecht University
28 June 2019

Image on the cover: Voronoi diagram of a set of points, representing biological cells. Points represent cell nuclei and Voronoi domains represent cells, with polygon edges standing for cellular membranes.

Abstract

Tissue mechanics controls biological processes such as cancer metastasis, embryonic development and wound healing. Recent studies have examined jamming transitions in tissues to determine how they become fluid-like, which is considered key to understanding these phenomena. Here, two models of biological cells are used to describe the dynamics of epithelial tissue and to study the effect of oscillations on the onset of flow in tissues. The first model treats cells as soft deformable disks interacting via the Hertz potential and imposes oscillations in the size of the particles. The second model describes cells as polygons through a Voronoi diagram, allowing changes in size and shape. We found that oscillations in diameter enhance motion of crystallised 'Hertzian cells' and hinder the motion of cells in dense tissues. The Voronoi model was implemented with a flip algorithm, but stability issues were found. Further analysis of these issues is required to investigate the role of shape oscillations in fluidisation of the tissue as described by the Voronoi model.

Contents

1 Introduction 5

2 Background 7

2.1 Epithelial Tissue . . . 7

2.2 Physics of Biological Tissues . . . 8

2.3 Models of Cell Dynamics . . . 10

2.4 Jamming and Glass Transitions . . . 12

2.5 T1 Topological Transitions . . . 12

2.6 Oscillations in Cell Size and Shape . . . 13

3 Methods 15

3.1 Vertex Model . . . 15

3.1.1 Shape Index . . . 17

3.1.2 Equations of Motion . . . 17

3.2 Voronoi Model 19

3.2.1 Voronoi Diagram and Delaunay Triangulation 20

3.2.2 Force Projection 22

3.2.3 Implementation of a Voronoi Diagram 23

3.2.4 Flip Algorithm 24

3.2.5 Activity 26

4 Toy Models **27**

4.1 Types of Dynamics 27

4.1.1 Integration Schemes 31

4.2 Neighbour Lists 33

4.3 Hertz Potential 35

4.4 Results 35

4.4.1 Passive Hertzian Particles 36

4.4.2 Active Hertzian Particles 38

4.4.3 Hertzian Particles Oscillating 40

4.4.4 Active Hertzian Particles Oscillating 43

5 Voronoi Model **47**

5.1 Voronoi Diagram 47

5.2 Barycentric Coordinates 50

5.3 Flip Algorithm 50

5.4 Triangular Lattice with Displaced Row 51

6 Conclusion **55**

Chapter 1

Introduction

Cancer metastasis, embryonic development and wound healing are biological processes for which cell dynamics is important. Collective properties are proposed to play a role in these phenomena [1], specifically for the fluidisation of the tissue, which is related to jamming and glass transitions. Experimental studies have shown that epithelial cells can undergo glass transitions and form an amorphous solid [2]. Cells can also change size and shape through contractions and extensions of the cytoskeleton and its associated protein filaments [3]. It has been observed that cells in epithelial tissue contract and expand in a coordinated fashion [4]. Recently, computational studies of tissue models have reported a rigidity transition upon changing an internal parameter that describes the elongation of the cells [5]. The aim of this thesis is to contribute to this discussion and to explore the influence of cellular size and shape oscillations on the fluidisation of epithelial tissues, by asking whether oscillations enhance cell motility.

To answer this question, two models were studied. First, the Hertzian potential was used as a toy model, describing cells as deformable soft disks with short range interactions. Simulations at different densities were performed and the size of the particles was made to oscillate sinusoidally with different amplitudes, frequencies and phases. The second model that was implemented was the one used by Bi et al. [5], the Voronoi model. This framework describes cells as polygons that interact with their immediate neighbours according to geometric variables, namely area and perimeter, which express mechanical properties such as tension and contractility. In the Voronoi model, oscillations in size and shape are possible.

The diffusion coefficient of the Hertzian disks was used as a measure of cell motility. We found that diameter oscillations in a low density fluid phase have no effect on diffusivity, while at high density they hinder motion. Conversely, oscillations enhance motion in a crystallised arrangement. The Voronoi model was implemented and features of the flip algorithm were validated. However, stability issues not yet fully understood impeded the study of oscillations.

This thesis starts with a conceptual introduction to epithelial tissue, in Chapter 2, as well as the motivation to study this biological subject from a physical point of view. Chapter 3 deals with the details of the Voronoi model and its simpler counterpart, the vertex model. The toy model that describes cells as Hertzian particles is explored in Chapter 4, and results of the Voronoi model are presented in Chapter 5. Chapter 6 presents the conclusions of this project, as well as possible directions of further studies.

Chapter 2

Background

2.1 Epithelial Tissue

There are four basic types of tissue in animals: epithelial, muscle, connective and nervous tissue [6]. Epithelial tissue covers the outside of the body and lines organs and cavities. It is made up of closely packed epithelial cells, which form a mechanical barrier. This dense packing leads to confluent configurations, where cells are arranged in a dense layer, with no empty spaces between them. In such configurations, protein complexes called cell junctions establish contact between adjacent cells.

Epithelial cells can have different shapes, according to their function. Those that are large and brick-shaped are called columnar epithelial cells and facilitate secretion and active absorption. They are found, for example, in the intestines, where digestive juices are secreted and nutrients absorbed. Squamous epithelial cells are plate-like and form thin layers whose function is the exchange of chemicals via diffusion. They line blood vessels and pulmonary alveoli, where they diffuse nutrients and oxygen. Cuboidal epithelial cells are dice-shaped and form most glands and glandular tubules of the body, where they help with secretion.

The study of epithelial tissue is useful due to the insights it can provide about carcinoma and organogenesis. Carcinomas are cancers that originate in epithelial cells [7]. Because epithelial tissue lines organs and glands, a significant number of the most common cancers are carcinomas. Specifically, all prostate and pancreatic cancers and nearly all lung, oral and breast cancers arise from malignant mutations in epithelial cells.

Organogenesis is a step in embryonic development during which the three primary cell layers of an embryo (endoderm, mesoderm and ectoderm) give rise to all four fundamental tissues and all organs of an animal [8]. This process involves cell differentiation and tissue flows, that spatially arrange cells to form different body structures. Thus, studying epithelial tissue can help understand not only how cancer develops and spreads but also how tissues move during embryonic development to form organs.

2.2 Physics of Biological Tissues

Biological cells are highly complex systems composed of many different structures and signalling networks and, as such, cellular processes are primarily studied from a single-cell perspective. However, there are cases where higher-level physical properties become relevant, especially when studying biological tissues like epithelia, where a large number of cells come together, and when studying disease progression, for which cell mechanics is important.

To assess the role of tissue-level properties, let us consider the stiffness-softness paradox of tumours [1]. On the one hand, magnetic resonance elastography shows that tumours are stiffer than surrounding tissue, allowing their detection as lumps [9]. On the other hand, optical deformability studies show that tumour cells are softer — their cytoskeletons are more deformable — than non-cancerous cells [10], which facilitates cancer invasion since softer cells can more easily travel across thin gaps in the extra-cellular matrix and in the walls of blood vessels [11]. Thus, stiff tumours contain softer cells. This contradiction between single-cell and tissue-level properties points towards a role of emergent phenomena.

Another motivation for studying the mechanics of tissue biology is the fact that, in epithelia, a change in cell-cell adhesion and cell contractility gives rise to the epithelial-mesenchymal transition (EMT) [1]. This transition corresponds to a transformation of phenotype, whereby polarised epithelial cells become elongated mesenchymal stem cells, with enhanced migration and invasiveness [12]. Mesenchymal stem cells are connective tissue cells that are multipotent and can therefore differentiate into several cell types [13]. Because EMT is associated with a transition from collective movement to single cell movement, it is proposed to be critical for tumour progression and cancer metastasis, especially in carcinomas [14, 15]. It also plays an important role in other processes, such as tissue repair [16] and inflammation [17].

Cellular tissues lend themselves to physical studies because they are viscoelastic, behaving as elastic solids or as viscous fluids in different circumstances [1]. Tissues are reminiscent of fluids, namely immiscible ones, when different types of cells coexist and sort themselves into different domains [18]. Elasticity, in turn, is present when, for example, tissues are moulded into spheres and are observed to respond elastically to deformations [19], analogously to elastic liquid droplets. Surface tension is at the origin of both these phenomena. Elasticity is due to the resistance that the macroscopic surface tension offers to deformations. Furthermore, cellular surface tension leads to sorting because it varies according to the magnitude of the microscopic interactions: assymetry in the interactions between constituents of the same cell and between constituents of different cells originates different surface tensions and thus different macroscopic spatial preferences. A variety of mechanisms are proposed to give rise to tissue surface tension [1]: cell-cell adhesion, mediated by molecules called cadherins; cell contractility, mediated by the actin cortex of cells, which is adjacent to the cytoskeleton; or a combination of the two, since cadherins are coupled to the actin cortex. A final reason to study tissues using tools from physics is the fact that cells consume energy and create active forces, which prompts their study as active fluids instead of simple, passive ones.

2.3 Models of Cell Dynamics

There are various approaches to studying the mechanics of cells. All of them can be simulated in two dimensions, instead of three, without loss of generality, since, as mentioned in section 2.1, epithelial tissue consists of thin layers. Discrete models, that describe cells individually, can be divided in roughly three types, based on the way they treat interactions between cells. These models use particle-like potentials, update rules or geometry-based local forces [20].

The first category includes models ranging from those that treat cells as simple particles to those that describe internal cellular details. Cells as particles can be modelled in isolation or in confluent tissues and can be deformable [21] and asymmetric [22]. Models with intra-cellular components calculate the interactions not only between cells but also between constituents of the cells, such as the particles that make up the membrane [23].

The second category features mainly the cellular Potts model. This approach employs a spatial lattice, where each point belongs to a particular cell or to interstitial fluid and changes its state according to a Monte Carlo-like rule [24]. There are no explicit forces in the cellular Potts model, only an energy associated to each state that the system seeks to minimise. Thus, the evolution does not follow Newtonian mechanics, unlike the models in the other categories, which evolve with explicit equations of motion, integrated computationally using molecular dynamics (MD) algorithms.

The third category contains vertex models and phase field models. Vertex models describe each cell as a polygon, with edges representing the membranes that separate neighbouring cells. Interactions are calculated locally using the area and perimeter of adjacent cells to quantify biological features such as cell volume incompressibility, cellular contraction and membrane tension [25]. Phase field models, on the other hand, represent each cell as a moving interface, characterized by a phase field that transitions from one inside the cell to zero outside of it [26]. Interactions rely on the perimeter and curvature of the membranes, as well as overlaps between cells.

Apart from these discrete models, there are also continuum models, that use a cell concentration instead of describing each cell individually [27]. Continuum models consist of partial differential equations, in space and time, for cell concentration, velocity and polarity, as well as inter-cellular adhesion. Adhesion is in some cases described using Maxwell's theory of viscoelastic fluids [28].

To describe confluent tissues and simulate the collective motion of cells, vertex models arise as the most appropriate tool, due to their low computational cost, the natural description of cell shapes, as can be seen in Fig. 2.1, and the fact that they favour topological aspects of the distribution of cells, instead of focusing on intra-cellular details.

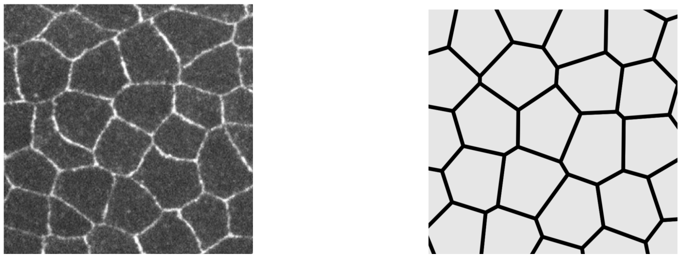

(a) *Epithelial tissue.* (b) *Voronoi diagram.*

Figure 2.1: *Voronoi tessellations as a representation of epithelial tissue. Microscopy image from [29], licensed under CC BY IGO.*

Vertex models can be further distinguished from Voronoi models [5], where cells are represented not as generic polygons but as Voronoi domains of the cell nuclei. A Voronoi diagram of a discrete set of points divides space into regions, also called Dirichlet domains or Wigner-Seitz cells, that contain all the locations closer to that point than to any other point in the set. The main difference between vertex and Voronoi models is that the equations of motion of the former describe the dynamics of the vertices of the polygon, whereas in the latter the equations of motion pertain to the cell centres.

Both models have been used to describe wound healing, cell sorting [30] and tissue folding and growth [31]. Recently, studies using the Voronoi model proposed the existence of a jamming transition in cell dynamics [5], which can be important for the epithelial-to-mesenchymal transition, introduced in section 2.2.

2.4 Jamming and Glass Transitions

Jamming transitions correspond to abrupt dynamical arrest and occur in non-biological systems, such as granular materials, foams and traffic jams, when the density is increased beyond a certain point [32]. Glass transitions occur in amorphous materials when the temperature decreases and changes the consistency of the material, from a viscous liquid to a crystal state [33]. Jamming and glass transitions are similar in the sense that they restrict the system to a small region of phase space, either by varying the density or the temperature, respectively.

These rigidity transitions have been studied in the context of biology for phenomena in which cell motility, and therefore cell arrest, is relevant [1]. Cell arrest corresponds to the equilibrium, non-perturbed configuration of the tissue, when cells are jammed and do not move significantly. Contrarily, cell motility coincides with a fluidised state, where cells have inhanced displacements. However, in contrast to jamming and glass transitions in granular matter, biological tissues often have constant temperature and a constant volume fraction of one, due to being confluent. Therefore, jamming and glassy behaviour are proposed to occur in tissues as a result of factors other than temperature or density. Some of the variables suggested to trigger and regulate rigidity transitions in cellular tissue are active motility, cell contractility, cell shape, applied stress, and cell-cell adhesion [1]. Nevertheless, it is still debated whether density plays a role in cellular jamming [34]. A glass transition due to cell-cell and cell-substrate adhesion has been observed in an aging epithelial monolayers by Garcia et al. [2].

2.5 T1 Topological Transitions

In confluent tissue like epithelia, cells are, as seen in Fig. 2.1, approximately polygons that occupy the entire two-dimensional layer, sharing edges with their immediate neighbours. When one cell moves persistently in one direction and is able to overcome the energy barrier imposed by its neighbours, it breaks the cell junctions in front of it, inserting itself where once was an edge between two other cells. This is called a T1 topological transition.

In a T1 transition, tissue topology changes locally through the exchange of neighbours between four cells. As shown in Fig. 2.2, cells that share an edge (the white cells in the figure), and are thus neighbours, are drawn apart until they only share a single vertex (in red in the picture). By moving them further away from each other, the single vertex splits into two vertices, connected by a horizontal edge shared by the green and blue cells. Thus, two cells that were neighbours no longer are and two cells that were not neighbours now share an edge. Furthermore, an edge that was vertical (orange) collapsed into a point (red), shared by all four cells, and then flipped into a horizontal edge (yellow).

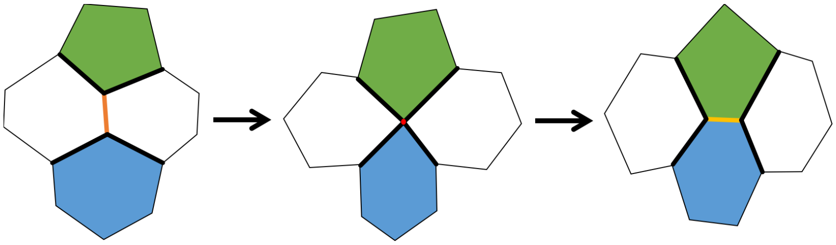

Figure 2.2: *T1 topological transition, necessary for tissue rearrangement.*

Since this is the only way cells can move around in confluent tissue, T1 transitions are a necessary condition for and a measure of cell motility and tissue fluidity.

2.6 Oscillations in Cell Size and Shape

Oscillations in cell area are driven by transient actin-myosin accumulations in the cell cortex, which change the large-scale actin and myosin structures of the cell [4]. Cell shape oscillations also arise due to rearrangements of actin and myosin, as well as microtubules, caused by changes in substrate adhesion or by biochemical cues [35]. Both types of oscillations can be autonomous [3], that is, a consequence of single-cell processes and not collective properties.

Numerous studies have addressed tissue-level oscillations, caused by changes at the tissue boundary [36] or shear deformations [37], but work on single cell oscillations in confluent tissue has been scarce and focused solely on aspects such as fluctuations of junction tension [29], and not on oscillations of size and shape, which are the focus of this thesis.

Chapter 3

Methods

This chapter gives details on two models introduced in section 2.3: the vertex model and the Voronoi model. The vertex model is introduced first as it is mathematically simpler but very similar to the Voronoi model. Then the Voronoi model is briefly described, before an explanation of the Voronoi digram and its dual tessellation, the Delaunay triangulation, which are a necessary ingredient to derive the equations of motion. The rest of the chapter deals with practical aspects of the implementation: how the Voronoi diagram is calculated, how the simulation can be sped up with the flip algorithm and how activity can be incorporated in the motion of the cells.

3.1 Vertex Model

The vertex model treats a confluent tissue as a convex polygonal partitioning of space, where the degrees of freedom are the vertices of each polygon. The energy of a system of N polygons is defined as

$$E = \sum_{i=1}^{N} \frac{K_i}{2}(A_i - A_i^0)^2 + \sum_{i=0}^{N} \frac{\Gamma_i}{2}(P_i - P_i^0)^2, \tag{3.1}$$

where A_i and P_i are the area and perimeter of cell i, and A_i^0 and P_i^0 are constants denoting the target area and target perimeter of that cell. Finally, K_i and Γ_i are elastic moduli quantifying how hard it is to modify the area and the perimeter of cell i [20].

The first term of Eq. 3.1 represents cell volume incompressibility and the resistance of the epithelial monolayer to height fluctuations. The second term stands for contractility of the actin-myosin cortex and cell membrane tension due to cell-cell adhesion and cortical tension [5]. Cell membrane tension is linear in perimeter and incorporated in the above expression by assuming that the tension modulus at each junction is equal for all junctions belonging to the same cell [30].

The area and perimeter of each polygon are calculated from the positions of its vertices:

$$A_i = \frac{1}{2}\sum_{\mu\in\Omega_i}(\vec{r_\mu} \times \vec{r}_{\mu+1}) \cdot \hat{N}_i, \qquad P_i = \sum_{\mu\in\Omega_i} |\vec{r}_{\mu+1} - \vec{r}_\mu|, \tag{3.2}$$

with $\hat{N}_i = \hat{e_z}$ a unit-length vector perpendicular to the surface of the polygon. The sums are counter-clockwise over all vertices μ that belong to polygon Ω_i, closing the loops with $\mu + 1 \equiv 1$ for $\mu = N_{\Omega_i}$.

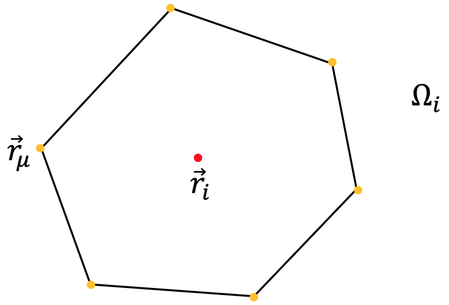

Figure 3.1: *Polygon* Ω_i *with centre* $\vec{r}_i$*, in red, and vertices* $\vec{r}_\mu$*, in yellow.*

3.1.1 Shape Index

A dimensionless ratio can be defined from the target area and the target perimeter of the cells:

$$f_i^0 = \frac{P_i^0}{\sqrt{A_i^0}}. \tag{3.3}$$

This ratio describes shape. The shape ratios of some geometric figures are presented in Table 3.1. Elongated polygons, like an ellipse with large aspect ratio (for example, $a/b = 3$), have higher shape ratios.

Polygon	A	P	f
circle	πr^2	$2\pi r$	≈ 3.54
pentagon	$5\ell^2/4\tan(\pi/5)$	5ℓ	≈ 3.81
ellipse, $a = 2b$	$2\pi b^2$	$\approx \sqrt{10}\pi b$	≈ 3.96
square	ℓ^2	4ℓ	4
ellipse, $a = 3b$	$3\pi b^2$	$\approx \sqrt{20}\pi b$	≈ 4.58

Table 3.1: *Area, perimeter and shape index f of some geometric figures. The perimeter of an ellipse was approximated by $P \approx 2\pi\sqrt{(a^2+b^2)/2}$, with a and b the major and minor axes.*

The jamming transition found in Ref. [5] occurs when the shape index increases and cells become elongated. Specifically, the transition is observed at $f^0 \approx 3.81$. In fact, an increase in f^0 corresponds to cortical tension dominating over cell-cell adhesion, which facilitates fluidisation of the tissue [1]. The value of f^0 for which the transition occurs decreases when cells are self-propelled, or active (see section 3.2.5).

3.1.2 Equations of Motion

In the overdamped limit, where inertial effects are insignificant and the second derivative of the position can be ignored, the equation of motion of each vertex is

$$\gamma \frac{d\vec{r}_\mu}{dt} = \vec{F}_\mu, \tag{3.4}$$

with $\vec{r}_\mu$ the position of vertex μ, $\vec{F}_\mu$ the force on that vertex and γ a friction coefficient. Forces are obtained from the energy as

$$\vec{F}_\mu = -\vec{\nabla}_{\vec{r}_\mu} E = -\sum_{i=1}^{N} \left[K_i (A_i - A_i^0) \vec{\nabla}_{\vec{r}_\mu} A_i + \Gamma_i (P_i - P_i^0) \vec{\nabla}_{\vec{r}_\mu} P_i \right], \tag{3.5}$$

where $\vec{\nabla}_{\vec{r}_\mu}$ is the gradient with respect to the coordinates of vertex μ. The gradients of the area and perimeter are obtained using Eq. 3.2:

$$\vec{\nabla}_{\vec{r}_\mu} A_i = \frac{1}{2} \left(\vec{r}_{\mu+1} - \vec{r}_{\mu-1} \right) \times \hat{N}_i \tag{3.6}$$

$$\vec{\nabla}_{\vec{r}_\mu} P_i = \frac{\vec{r}_\mu - \vec{r}_{\mu-1}}{|\vec{r}_\mu - \vec{r}_{\mu-1}|} - \frac{\vec{r}_{\mu+1} - \vec{r}_\mu}{|\vec{r}_{\mu+1} - \vec{r}_\mu|}. \tag{3.7}$$

Thus, the expression of the force on each vertex is

$$\begin{aligned} \vec{F}_\mu = & -\sum_{i=1}^{N} \frac{K_i}{2} (A_i - A_i^0) \left(\vec{r}_{\mu+1} - \vec{r}_{\mu-1} \right) \times \hat{N}_i \\ & -\sum_{i=1}^{N} \Gamma_i (P_i - P_i^0) \left(\frac{\vec{r}_\mu - \vec{r}_{\mu-1}}{|\vec{r}_\mu - \vec{r}_{\mu-1}|} - \frac{\vec{r}_{\mu+1} - \vec{r}_\mu}{|\vec{r}_{\mu+1} - \vec{r}_\mu|} \right), \end{aligned} \tag{3.8}$$

where the sums over polygons i are effectively only over the polygons that share vertex μ. Vertex $\mu - 1$ is the vertex before μ in cell i, in counter-clockwise order, and vertex $\mu + 1$ is the one that comes after vertex μ.

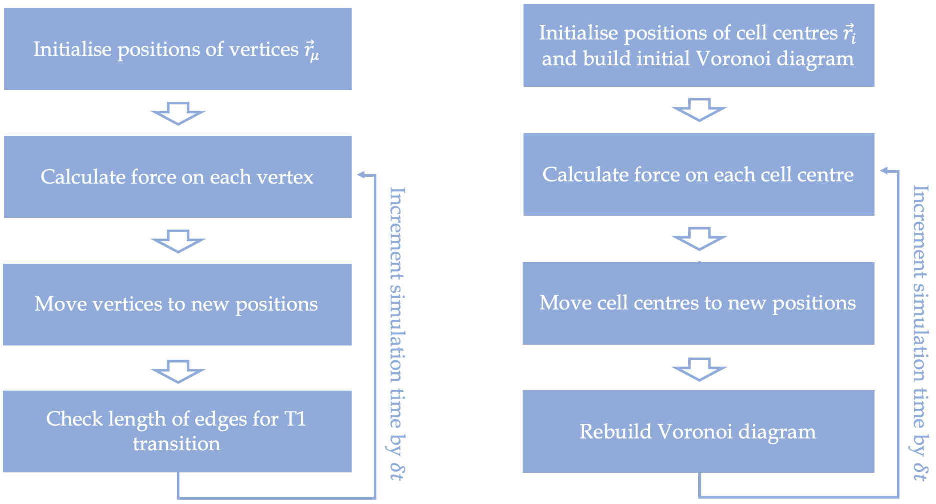

(a) *Vertex model.* (b) *Voronoi model.*

Figure 3.2: *Flow chart of the vertex and Voronoi model algorithms.*

Calculating the dynamics of cells in the vertex model corresponds to following the steps in Fig. 3.2a. An initial tessellation of polygons is generated, defining the initial coordinates of the vertices, $\vec{r}_\mu$. The initial velocity of each vertex is also set. Then, at each time step, the force on each vertex is calculated according to Eq. 3.8. Using the newly calculated forces and the velocities of each vertex, new positions $\vec{r}_\mu$ are calculated by integrating the equations of motion, Eq. 3.4. T1 topological transitions take place when the length of an edge falls below a threshold. Implementing a T1 transition is similar to performing a flip in the Voronoi model, which will be explained in section 3.2.4.

3.2 Voronoi Model

The Voronoi model is similar to the vertex model, except the degrees of freedom are the cell centres and not their vertices. Furthermore, the polygons that represent cells are Voronoi polygons, each generated by the cell centre it represents. The energy expression is precisely the same (Eq. 3.1) although now the expression of the force is different, because the gradient must be with respect to the coordinates of the central sites, $\vec{r_i}$. The equation of motion of each site i is:

$$\gamma \frac{d\vec{r_i}}{dt} = -\nabla_{\vec{r_i}} E. \tag{3.9}$$

Since cell areas and perimeters are calculated using the coordinates of the vertices $\vec{r_\mu}$, a relation between $\vec{r_\mu}$ and $\vec{r_i}$ is needed to calculate the projection of the force on the central sites. This relation comes from the properties of the Voronoi diagram and its dual, the Delaunay triangulation, explained in the next section.

The general algorithm of the Voronoi model is shown in Fig. 3.2b. The simulation starts by setting the initial coordinates of each cell centre, as well as their velocities. These positions are used as seed points for the Voronoi diagram. Calculating the Voronoi cell associated with each point determines the positions of the vertices. The vertex model can be initialised in exactly the same way, except then the positions of the cell centres are discarded and only the positions of the vertices are used for all subsequent calculations. The next step in the Voronoi model is to calculate the force on each cell centre. This is a lengthier calculation than in the vertex model, because, as mentioned, the force on the vertices must be projected onto the cell centres. Then, using an integration scheme, new positions for the centres are calculated. From here, the new positions of the vertices are found by updating the Voronoi diagram according to the new positions of the seed points.

3.2.1 Voronoi Diagram and Delaunay Triangulation

As mentioned in section 2.3, a Voronoi diagram of a set of points is defined as the partition of space into domains whose points are closer to the seed point of that domain than to any other seed in the set. The dual graph of the Voronoi diagram for the same set of seed points is the Delaunay triangulation, defined as the partition of space into triangles, whose vertices are the seed points, such that no seed point is inside the circumcircle of any triangle.

The circumcentres of the Delaunay triangles are the vertices of the Voronoi cells. Thus, every site (cell center) is associated with a Voronoi polygon and every vertex corresponds to a Delaunay triangle. Furthermore, if two Delaunay triangles share an edge, their circumcentres are connected with an edge in the Voronoi tessellation.

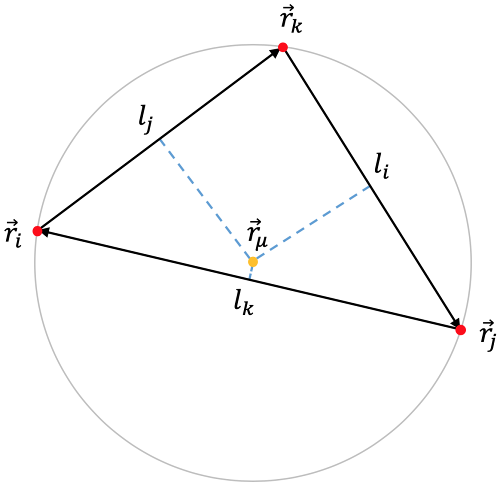

Figure 3.3: *Triangle with vertices* i, j *and* k, *in red, and circumcentre* μ, *in yellow.*

The position of the circumcentre, $\vec{r}_\mu$, is related to the positions of the vertices of a triangle, $\vec{r}_i$, $\vec{r}_j$ and $\vec{r}_k$ (see Fig. 3.3), by

$$\vec{r}_\mu = \frac{\lambda_i}{\Lambda}\vec{r}_i + \frac{\lambda_j}{\Lambda}\vec{r}_j + \frac{\lambda_k}{\Lambda}\vec{r}_k, \tag{3.10}$$

where $\Lambda = \lambda_i + \lambda_j + \lambda_k$ and λ_i, λ_j and λ_k are the barycentric coordinates, given by

$$\lambda_i = l_i^2(l_j^2+l_k^2-l_i^2), \qquad \lambda_j = l_j^2(l_k^2+l_i^2-l_j^2), \qquad \lambda_k = l_k^2(l_i^2+l_j^2-l_k^2), \tag{3.11}$$

with

$$l_i = |\vec{r}_j - \vec{r}_k|, \qquad l_j = |\vec{r}_k - \vec{r}_i|, \qquad l_k = |\vec{r}_i - \vec{r}_j|. \tag{3.12}$$

3.2.2 Force Projection

Calculating the gradient in Eq. 3.9 involves applying the chain rule to the gradients of the area and of the perimeter:

$$[\nabla_{\vec{r}_i} A_i]_k = \sum_{\mu\in\Omega_i} [\nabla_{\vec{r}_\mu} A_i]_m \left[\frac{\partial \vec{r}_\mu}{\partial \vec{r}_i}\right]_{mk}, \quad [\nabla_{\vec{r}_i} P_i]_k = \sum_{\mu\in\Omega_i} [\nabla_{\vec{r}_\mu} P_i]_m \left[\frac{\partial \vec{r}_\mu}{\partial \vec{r}_i}\right]_{mk}. \tag{3.13}$$

Therefore, one needs to calculate the Jacobian $\frac{\partial \vec{r}_\mu}{\partial \vec{r}_i}$ for each vertex, which is a novelty of the Voronoi model. The gradients $\nabla_{\vec{r}_\mu} A_i$ and $\nabla_{\vec{r}_\mu} P_i$ were already present in the vertex model (Eqs. 3.6 and 3.7).

Using the expression for $\vec{r}_\mu$ in terms of the barycentric coordinates (Eq. 3.11), the Jacobian is:

$$\begin{aligned}
\frac{dx_\mu}{dx_p} &= \frac{1}{\Lambda}\left[\lambda_p + x_i\frac{d\lambda_i}{dx_p} + x_j\frac{d\lambda_j}{dx_p} + x_k\frac{d\lambda_k}{dx_p}\right] - \frac{x_i\lambda_i + x_j\lambda_j + x_k\lambda_k}{\Lambda^2}\frac{d\Lambda}{dx_p}\\
\frac{dx_\mu}{dy_p} &= \frac{1}{\Lambda}\left[x_i\frac{d\lambda_i}{dy_p} + x_j\frac{d\lambda_j}{dy_p} + x_k\frac{d\lambda_k}{dy_p}\right] - \frac{x_i\lambda_i + x_j\lambda_j + x_k\lambda_k}{\Lambda^2}\frac{d\Lambda}{dy_p}\\
\frac{dy_\mu}{dx_p} &= \frac{1}{\Lambda}\left[y_i\frac{d\lambda_i}{dx_p} + y_j\frac{d\lambda_j}{dx_p} + y_k\frac{d\lambda_k}{dx_p}\right] - \frac{y_i\lambda_i + y_j\lambda_j + y_k\lambda_k}{\Lambda^2}\frac{d\Lambda}{dx_p}\\
\frac{dy_\mu}{dy_p} &= \frac{1}{\Lambda}\left[\lambda_p + y_i\frac{d\lambda_i}{dy_p} + y_j\frac{d\lambda_j}{dy_p} + y_k\frac{d\lambda_k}{dy_p}\right] - \frac{y_i\lambda_i + y_j\lambda_j + y_k\lambda_k}{\Lambda^2}\frac{d\Lambda}{dy_p},
\end{aligned}$$

where $p = i, j, k$, according to Fig. 3.3. The 24 derivatives of λ_p and Λ with respect to x_p and y_p can be calculated straightforwardly from Eqs. 3.11 and 3.12. Details of these calculations can be found in [30].

The equation of motion for each cell is then

$$\gamma\frac{d\vec{r}_i}{dt} = -\sum_{k=1}^{N}\frac{K_k}{2}(A_k - A_k^0)\sum_{\mu\in\Omega_k}\left[(\vec{r}_{\mu+1}-\vec{r}_{\mu-1})\times\hat{N}_k\right]^T\left[\frac{\partial\vec{r}_\mu}{\partial\vec{r}_i}\right] \tag{3.14}$$
$$-\sum_{k=1}^{N}\Gamma_k(P_k - P_k^0)\sum_{\mu\in\Omega_k}\left(\frac{\vec{r}_\mu-\vec{r}_{\mu-1}}{|\vec{r}_\mu-\vec{r}_{\mu-1}|}-\frac{\vec{r}_{\mu+1}-\vec{r}_\mu}{|\vec{r}_{\mu+1}-\vec{r}_\mu|}\right)^T\left[\frac{\partial\vec{r}_\mu}{\partial\vec{r}_i}\right].$$

In practice, this means that, to calculate the total force on cell i coming from the area, one must calculate the factor $\frac{K_i}{2}(A_i - A_i^0)$ and multiply it by the sum, over all vertices of cell i, $\sum_{\nu\in\Omega_i}[(\vec{r}_{\nu+1}-\vec{r}_{\nu-1})\times\hat{N}_i]^T\left[\frac{\partial\vec{r}_\nu}{\partial\vec{r}_i}\right]$. Then, for each immediate neighbour j of cell i, the factor $\frac{K_j}{2}(A_j - A_j^0)$ is calculated and multiplied with the sum, over vertices of j that also belong to i, $\sum_{\nu\in\Omega_i\cap\Omega_j}[(\vec{r}_{\nu+1}-\vec{r}_{\nu-1})\times\hat{N}_j]^T\left[\frac{\partial\vec{r}_\nu}{\partial\vec{r}_i}\right]$. An analogous procedure is followed to calculate the perimeter contribution [30].

3.2.3 Implementation of a Voronoi Diagram

The Voronoi diagram of a set of points in two dimensions can be obtained with Fortune's algorithm, which sweeps the plane in the vertical or horizontal direction and draws the edges of the Voronoi cells as it goes through the sites by calculating the points that are equidistant to neighbouring sites. A thorough explanation can be found in [38]. For this project, an implementation of Fortune's algorithm in C, written by Mathias Westerdahl, was used [39].

After initialising the Voronoi diagram, linked lists were built to account for the connectivity between cell centres and vertices. Thus, for each cell centre there is a linked list of its Voronoi vertices and a linked list of the cell centres that are its direct neighbours, that is, that share a vertex with it. In turn, for every Voronoi vertex there is a linked list of the vertices of its Delaunay triangle and a linked list of its neighbouring triangles. The list of Voronoi vertices is used to calculate areas, perimeters and forces and the list of Delaunay vertices is used to calculate the barycentric coordinates. The list of Voronoi neighbours is used to calculate the force, for which only adjacent cells contribute, and the list of Delaunay neighbours is used in the flip algorithm, explained below.

3.2.4 Flip Algorithm

At each iteration of the integration of the Voronoi system, the last step is to rebuild the Voronoi diagram, that is, to update the vertices' positions from the newly calculated cell centre positions. This can be done in two ways. The first approach [5] recalculates the Voronoi diagram from scratch, using as seeds the new positions of the sites. The second approach [30] is the flip algorithm, which sweeps the diagram and looks for places where an edge of the Delaunay triangulation needs to be flipped in order to keep the tessellation strictly Delaunay (and its dual strictly Voronoi). In this approach, once the diagrams are updated, the positions of the vertices are calculated using the barycentric coordinates, Eq. 3.10. Therefore, the flow chart of the Voronoi model with the flip algorithm is the one in Fig. 3.5.

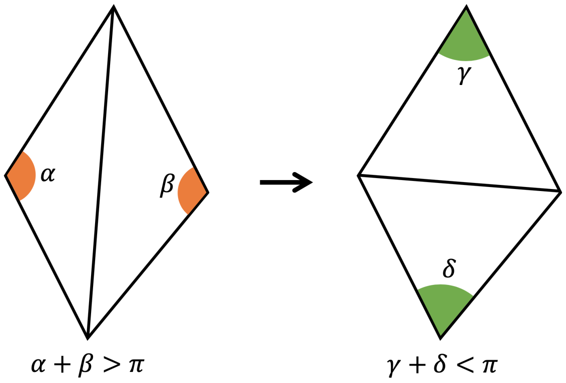

Figure 3.4: *Equiangulation procedure: for every pair of adjacent Delaunay triangles, if $\alpha + \beta > \pi$, the edge of the triangles is flipped.*

The flip algorithm computes, for every edge of the triangulation, the sum of the angles opposite to it. If the sum is larger than π, the edge is flipped, connecting the two sites that were previously opposed — see Fig. 3.4. This corresponds to the T1 transition described in section 2.5. The procedure is repeated until there are no more edges to flip, at which point the triangulation is Delaunay, and its dual tessellation is Voronoi. This method, called equiangulation, carries a lower computational cost than calculating a full Voronoi diagram at each time step.

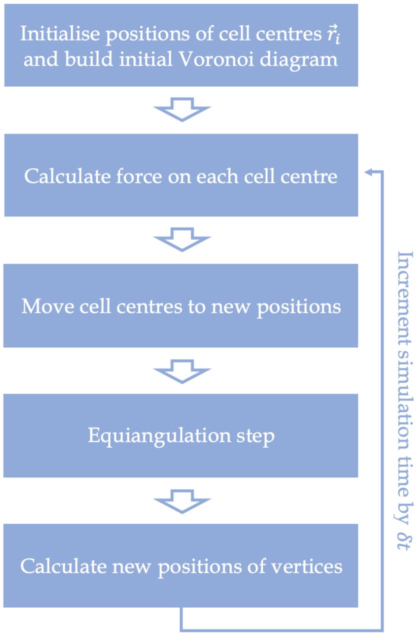

Figure 3.5: *Flow chart of the Voronoi model with the flip algorithm.*

Flipping an edge of the triangulation corresponds to updating most of the structures in the code. The exchange of Voronoi neighbours means that cells 1 and 3 (see Fig. 3.6) leave each other's neighbour lists and cells 2 and 4 become neighbours. Furthermore, there is loss and gain of Voronoi sites, i.e., the lists of vertices of cells 2 and 4 gain one element and those of 1 and 3 lose one. There is also a rearrangement of Delaunay neighbour lists. Finally, the list that keeps track of Delaunay edges needs to be updated so that the previous edge is erased and the new, flipped edge is created.

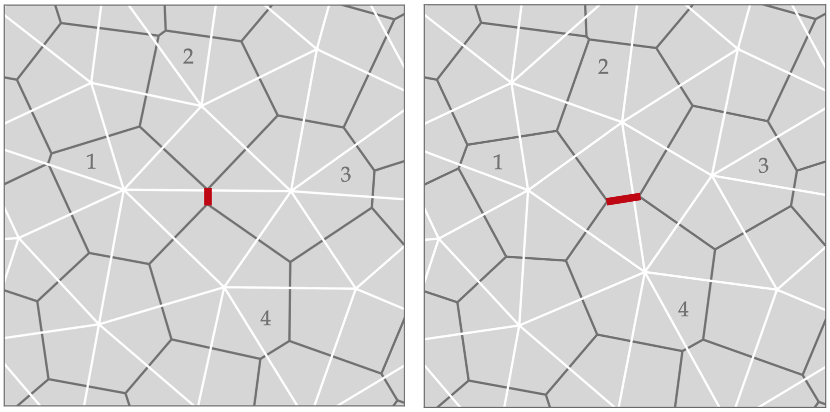

Figure 3.6: *Voronoi tesselation (in dark gray) and Delaunay triangulation (in white) during a T1 transition. Marked in red is the edge that flips during the transition.*

3.2.5 Activity

Self-propulsion can be incorporated in the Voronoi model to represent cell orientation. In the simplest case, orientation is treated as a unit vector that undergoes random rotational diffusion. The equation of motion of each cell is modified by activity thus:

$$\frac{d\vec{r}_i}{dt} = \frac{1}{\gamma}\vec{F}_i + v_o\hat{n}_i, \tag{3.15}$$

where $\hat{n}_i = (\cos\theta_i, \sin\theta_i)$ is the unit vector representing each cell's polarity and v_0 is the constant magnitude of the self-propulsion force [5]. The stochastic evolution of the polarity angle θ_i is described by

$$\frac{d\theta_i}{dt} = \eta_i(t), \tag{3.16}$$

with $\eta_i(t)$ a white-noise process with zero mean and variance $2D_r$ (see details in section 4.1), and D_r the rotational noise strength, which determines the persistence of $\hat{n}_i$. Activity cannot be easily incorporated in the vertex model because the degrees of freedom there are the vertices.

Chapter 4

Toy Models

4.1 Types of Dynamics

The evolution of the Voronoi model relies on a molecular dynamics (MD) algorithm, that is, an algorithm that explicitly integrates the equations of motion of all constituents of a system, yielding trajectories and thermodynamical quantities that are physically meaningful. The Voronoi model also incorporates activity, or self-propulsion, of the degrees of freedom. This means that energy enters the system through intrinsic velocity of the cells, and thus has to be dissipated. Furthermore, it is assumed that self-propulsion undergoes random reorientation, for which stochastic differential equations are needed.

In order to arrive at dissipative translational dynamics and stochastic rotational dynamics, several modifications need to be made to the initial energy-conserving implementation of molecular dynamics. The reason the NVE ensemble serves as starting point is that it is easiest to correct, since the energy is straightforward to calculate and needs to be strictly conserved throughout the simulation. To test the first integration scheme and the subsequent modifications to the dynamics, a system simpler than the Voronoi model was used, namely, a system of disk-like particles interacting via a two-particle potential. This potential was then used as a toy model for cellular tissue, discussed in sections 4.4.3 – 4.4.4.

After achieving an energy-conserving algorithm, a thermostat was added to obtain the equation of state of the system and confirm the validity of the integration. The thermostat ensures the temperature of the system is constant by introducing corrections to the velocities of the particles and thus forcing the kinetic energy to remain equal to a pre-set value. The Anderson thermostat does this by coupling the system to a heat bath through stochastic collisions between randomly selected particles and the heat bath, satisfying Maxwell-Boltzmann statistics [40]. Another possibility is the Nosé-Hoover thermostat, which is deterministic and uses an extended Lagrangian, with artificial coordinates and velocities, to introduce a thermodynamic friction coefficient. This coefficient measures the difference between the kinetic energy of the system and the kinetic energy associated with the desired temperature and corrects the force on each particle accordingly. At constant temperature, the pressure of the system is measured at different densities, yielding a curve $P(\rho)$.

When particles are suspended in a fluid, their collisions with the fast-moving molecules in the fluid give rise to Brownian motion, characterised by random fluctuations in a particle's trajectory. In the overdamped limit, where inertia is not relevant, and in a dissipative, viscous medium, the equation of motion for Brownian dynamics is

$$\gamma_t \frac{d\vec{r_i}}{dt} = \vec{F_i} + \vec{\xi_i}, \tag{4.1}$$

with γ_t the friction coefficient for translation, $\vec{F_i}$ the interaction force on particle i, and ξ_i a white-noise process that models the random fluctuations caused by collisions with the suspending particles. This process has, for each dimension (x and y), mean 0 and variance $2D_t\gamma_t^2$:

$$\langle \xi_i(t) \rangle = 0, \qquad \langle \xi_i(t)\xi_j(t') \rangle = 2D_t\gamma_t^2\delta(t-t')\delta_{ij},$$

where D_t is the translational diffusion coefficient. The translational diffusion coefficient is related to the translational friction coefficient via the temperature T: $D_t = k_BT/\gamma_t$, where k_B is the Boltzmann constant. The mean displacement of an isolated Brownian particle is 0 since, from the solution of

Eq. 4.1, with $\vec{F}_i = \vec{0}$, we have:

$$\langle \vec{r}_i(t) \rangle = \left\langle \vec{r}_i(0) + \frac{1}{\gamma_t} \int_0^t \vec{\xi}_i(t')dt' \right\rangle = \frac{1}{\gamma_t} \int_0^t \left\langle \vec{\xi}_i(t') \right\rangle dt' = 0.$$

The mean squared displacement, however, is non-zero. For a two-dimensional system, it is:

$$\begin{aligned}
\langle \vec{r}_i(t)\vec{r}_i(t) \rangle &= \frac{2\vec{r}_i(0)}{\gamma_t} \int_0^t \left\langle \vec{\xi}_i(t') \right\rangle dt' + \frac{1}{\gamma_t^2} \int_0^t \int_0^{t'} \left\langle \vec{\xi}_i(t'')\vec{\xi}_i(t''') \right\rangle dt''dt''' \\
&= \frac{1}{\gamma_t^2} \int_0^t \int_0^{t'} \left[\langle \xi_i^x(t'')\xi_i^x(t''') \rangle + \langle \xi_i^y(t'')\xi_i^y(t''') \rangle \right] dt''dt''' \\
&= \frac{2}{\gamma_t^2} \int_0^t \int_0^{t'} 2D_t\gamma_t^2 \delta(t'' - t''')dt''dt''' = 4D_t \int_0^t dt' \\
&= 4D_t t
\end{aligned} \tag{4.2}$$

Thus, the mean squared displacement of the particles in a diffusive system is linear in time and the diffusion coefficient can be obtained from a linear regression.

When Brownian particles are active, that is, when they have a self-propulsion force with constant magnitude and whose direction diffuses thermally, the translational equation of motion becomes:

$$\frac{d\vec{r}_i}{dt} = \frac{1}{\gamma_t}\left(\vec{F}_i + \vec{\xi}_i\right) + v_0\hat{n}_i,$$

where v_0 is the constant magnitude of the activity and $\hat{n}_i$ is the direction of each particle's self-propulsion. The self-propulsion $\hat{n}_i = (\cos\theta, \sin\theta)$ performs a rotational random walk in the plane:

$$\frac{d\theta_i}{dt} = \eta_i(t), \tag{4.3}$$

where η_i is the rotational white-noise process, with moments:

$$\langle \eta_i(t) \rangle = 0, \qquad \langle \eta_i(t)\eta_j(t') \rangle = 2D_r\delta(t - t')\delta_{ij}, \tag{4.4}$$

where D_r is the rotational diffusion coefficient, related to the temperature through $D_r = k_BT/\gamma_r$, with γ_r the rotational friction coefficient.

The mean squared displacement of an isolated active Brownian particle can be calculated by multiplying Eq. 4.1 (with $\vec{F}_i = \vec{0}$) by $\vec{r}_i(t)$, taking the ensemble average and then integrating over time:

$$\left\langle \vec{r}\frac{d\vec{r}}{dt} \right\rangle = \left\langle \frac{1}{2}\frac{d\left(\vec{r}^{\,2}\right)}{dt} \right\rangle = \frac{1}{2}\frac{d}{dt}\left\langle \vec{r}^{\,2} \right\rangle \Rightarrow \left\langle \vec{r}^{\,2}(t) \right\rangle = 2\int_0^t \left\langle \vec{r}(t')\frac{d\vec{r}(t')}{dt'} \right\rangle dt'.$$

The solution of Eq. 4.1 is $\vec{r}_i(t) = \vec{r}_i(0) + \frac{1}{\gamma_t}\int_0^t \left(\vec{\xi}_i(t') + v_0\hat{n}_i(t')\right) dt'$. We also have that $\langle \hat{n}_i(t)\cdot\hat{n}_i(t')\rangle = \exp\left(-2D_r(t-t')\right)$ (see derivation in Ref. [41]) and $\langle \xi_i(t) n_i(t)\rangle = 0$, that is, translational and rotational noise are uncorrelated. The calculation goes as follows:

$$\begin{aligned}
\frac{1}{2}\frac{d}{dt}\left\langle \vec{r}_i^{\,2} \right\rangle &= \frac{1}{\gamma_t}\int_0^t \left\langle \vec{\xi}_i(t)\cdot\vec{\xi}_i(t') \right\rangle dt' + v_0^2\int_0^t \left\langle \hat{n}_i(t)\cdot\hat{n}_i(t') \right\rangle dt' \\
&= \frac{2}{\gamma_t}2D_t\gamma_t^2\int_0^t \delta(t-t')dt' + v_0^2\int_0^t e^{-2D_r(t-t')}dt' \\
&= 2D_t + v_0^2 e^{-2D_r t}\int_0^t e^{2D_r t'}dt' \\
&= 2D_t + \frac{v_0^2}{2D_r}\left(1 - e^{-2D_r t}\right),
\end{aligned}$$

where we used the result $\int_0^t \delta(t-t')dt' = \frac{1}{2}$. Integrating over time to get $\langle \vec{r}_i^{\,2}(t)\rangle$ leads to:

$$\left\langle \vec{r}_i^{\,2}(t) \right\rangle = 4D_t t + \frac{v_0^2}{D_r}\int_0^t \left(1 - e^{-2D_r t'}\right) dt' = 4D_t t + \frac{v_0^2\tau_r^2}{2}\left(\frac{2t}{\tau_r} + e^{-2t/\tau_r} - 1\right),$$

where the rotational diffusion time $\tau_r = 1/D_r$ was introduced [42]. The term in parenthesis has two limiting cases, depending on whether $t \gg \tau_r$ or $t \ll \tau_r$:

$$\frac{2t}{\tau_r} + e^{-2t/\tau_r} - 1 = \begin{cases} \frac{2t}{\tau_r} & t \gg \tau_r \\ \frac{2t}{\tau_r} + \left(1 - \frac{2}{\tau_r}t + \frac{4}{\tau_r^2}t^2\right) - 1 & t \ll \tau_r \end{cases} = \begin{cases} \frac{2t}{\tau_r} & t \gg \tau_r \\ \frac{4t^2}{\tau_r^2} & t \ll \tau_r \end{cases}.$$

The mean squared displacement thus becomes:

$$\left\langle \vec{r}_i^{\,2}(t) \right\rangle = \begin{cases} 4D_t t + \frac{v_0^2}{D_r}t & t \gg \tau_r \\ 4D_t t + 2v_0^2 t^2 & t \ll \tau_r \end{cases}. \tag{4.5}$$

It is linear in time for long time scales, the diffusive regime, and quadratic for short times scales, the ballistic regime. From Eq. 4.5 it is possible to extract the effective translational diffusion coefficient:

$$D_{\text{eff}} = D_t + \frac{v_0^2}{2D_r}. \tag{4.6}$$

When particles have macroscopic size, they are no longer subject to thermal Brownian motion and form conglomerates of granular matter. The dynamics is dissipative:

$$\gamma_t \frac{d\vec{r}_i}{dt} = \vec{F}_i.$$

This is the relevant regime for biological cells (see Eqs. 3.4 and 3.9). However, as mentioned in section 3.2.5, when activity is introduced the equation of translational motion is changed to

$$\frac{d\vec{r}_i}{dt} = \frac{1}{\gamma_t}\vec{F}_i + v_0\hat{n}_i.$$

If the dynamics of $\hat{n}_i$ is assumed to be diffusive, that is, if cell orientation is assumed to be perturbed randomly by cellular processes and the environment, then cellular rotational dynamics is identical to that of active Brownian particles, and thus described by Eqs. 4.3 and 4.4.

4.1.1 Integration Schemes

Microcanonical Ensemble (NVE)

To realise an energy-conserving algorithm, a symplectic integration scheme, that is, an integration scheme for Hamiltonian systems, was chosen. The Velocity-Verlet scheme updates both the positions and the velocities of each particle and is a two-step algorithm because it calculates the new velocities both before and after updating the forces between particles.

$$\vec{x}(t+\Delta t) = \vec{x}(t) + \vec{v}(t)\Delta t + \frac{\vec{F}(t)}{2}\Delta t^2 \tag{4.7}$$

$$\vec{v}(t+\Delta t) = \vec{v}(t) + \frac{\vec{F}(t)+\vec{F}(t+\Delta t)}{2}\Delta t^2, \tag{4.8}$$

where the mass of the particles was set to 1.

Canonical Ensemble (NVT)

As mentioned in the previous section, one way to make an NVE integration NVT is to add a stochastic mechanism like the Anderson thermostat, whereby the particles collide with a heat bath and their velocities become thermalised. These collisions occur with frequency ν. As such, the probability that a particle is selected in a time step Δt to undergo a collision is $\nu\Delta t$. When a particle is selected [40], its velocity is updated to a value drawn from the Maxwell-Boltzmann distribution associated to the desired temperature:

$$\text{if } X_i(t) < \nu\Delta t : \quad \vec{v}_i(t) = \sqrt{k_B T}\vec{\Gamma}_i(t), \tag{4.9}$$

with $X_i(t)$ a random number between 0 and 1, drawn from a uniform distribution, and $\Gamma(t)$ a random number drawn from a Gaussian distribution.

The deterministic Nosé-Hoover thermostat introduces a friction coefficient ξ that imposes the correct kinetic energy by subtracting a frictional drag in the equation of motion [40]. The effective force on each particle i becomes $\vec{F}(t) - \xi(t)\vec{v}_i(t)$, with $\vec{F}_i$ the force calculated from the interaction potential and $\vec{v}_i(t)$ the velocity of particle i. The friction coefficient is updated through:

$$\xi(t + \Delta t) = \xi(t) + \frac{1}{Q}\left(\sum_i^N v_i^2(t) - dNT\right), \tag{4.10}$$

where d is the number of degrees of freedom and Q is a parameter from the extended Lagrangian and is usually set to 1.

Brownian Dynamics

To integrate the equations of motion of Brownian particles, a scheme appropriate to stochastic differential equations must be used. The Euler-Maru algorithm updates the positions of active particles at each time step according to:

$$\vec{x}(t+\Delta t) = \vec{x}(t) + \sqrt{2D_t}\,\vec{\Gamma}(t)\,\sqrt{\Delta t} + \frac{\vec{F}(t)}{\gamma_t}\Delta t + v_0\,\hat{n}(t)\Delta t,$$

where again $\Gamma(t)$ is a Gaussian random number. The orientation of each particle is updated as:

$$\theta(t+\Delta t) = \theta(t) + \sqrt{2D_r}\,\Gamma(t)\sqrt{\Delta t},$$

from which $\hat{n}$ is calculated: $\hat{n} = (\cos\theta, \sin\theta)$. According to Stokes' law, the friction coefficient on a particle of radius a moving in a fluid of viscosity η is $\gamma_t = 6\pi\eta a$. For rotational motion, the friction coefficient is given by[1] $\gamma_r = 8\pi\eta a^3$. For particles of diameter 1, we have that $\gamma_t/\gamma_r = 3$ and thus, recalling that $D = k_BT/\gamma$, $D_r = 3D_t$. The two equations become:

$$\vec{x}(t+\Delta t) = \vec{x}(t) + \sqrt{\frac{2k_BT}{\gamma_t}}\vec{\Gamma}(t)\sqrt{\Delta t} + \frac{\vec{F}(t)}{\gamma_t}\Delta t + v_0\,\hat{n}(t)\Delta t \tag{4.11}$$

$$\theta(t+\Delta t) = \theta(t) + \sqrt{\frac{6k_BT}{\gamma_t}}\,\Gamma(t)\sqrt{\Delta t}. \tag{4.12}$$

4.2 Neighbour Lists

In simulations with short ranged interactions, there is no need to calculate the forces between all pairs of particles, since particles that are at distances larger than the range of the potential will not feel each other's presence. These redundant pairs of interactions, when taken into account, significantly slow down the simulation, especially when the number of particles is high. Neighbour lists are a tool used to speed up the computation by performing a calculation that scales faster than N^2. In molecular dynamics simulations, they typically consist of a combination of cell lists and Verlet lists [40].

Implementing a cell list corresponds to dividing the simulation box in smaller boxes, or cells, of size r_c slightly larger than the cutoff radius of the potential, and then assigning particles to each cell according to their position. This is

---

[1] Other choices of γ_r can be made.

a calculation of order N. Using only cell lists, calculating the force on one particle would entail calculating its interaction with all the other particles in the same cell and in the neighbouring cells — 8 for a two-dimensional system.

The Verlet list of a particle is a list of all the particles whose distance to the original particle is smaller than the Verlet radius r_v, chosen to be larger than the cutoff radius. Calculating the force on one particle thus consists of calculating its interactions with all the particles in its Verlet sphere (or disk, in two dimensions). This a calculation of order N, whereas building a Verlet list is an operation of order N^2.

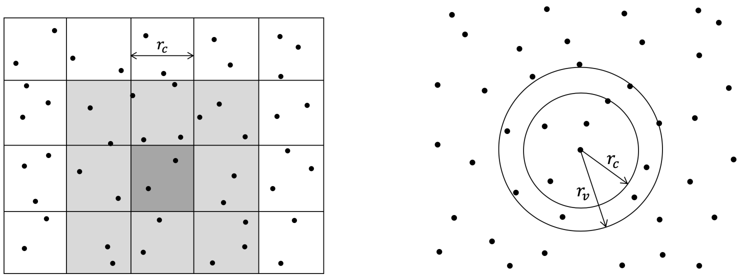

(a) *Cell list.* (b) *Verlet list.*

Figure 4.1: *Schematics of the construction of cell and Verlet lists, based on [40].*

Cell and Verlet lists are combined by employing cell lists to build Verlet lists and Verlet lists to calculate interactions. This way, the construction of Verlet lists is optimised, by taking into account only 9 cells instead of the whole box. Moreover, fewer redundant interactions are calculated, by looking only at a small circular region in space instead of 9 cells or, worse, the whole box. Using this combination, CPU time scales with N [40].

In this project, both lists were implemented using linked lists in C, one for each particle and one for each cell. The lists are maintained by updating them from scratch as soon as one particle is displaced more than $r_v - r_c$.

4.3 Hertz Potential

The Hertz potential describes the change in elastic energy of two deformable objects when subjected to axial compression [43]. This soft, repulsive potential has the form

$$V(r) = \begin{cases} \varepsilon\left(1 - \frac{r}{\sigma}\right)^{5/2} & r < \sigma \\ 0 & r \geq \sigma, \end{cases} \tag{4.13}$$

where ε is the maximum repulsion and σ is the range of the interaction.

This potential describes deformations and overlaps of round particles. As such, at high densities, Hertzian disks mimic the appearance of cells in a confluent tissue. Thus, the MD implementation of the Hertz potential was used as a toy model for the study of oscillations in the size of particles. To that end, a generalized form of the two-particle potential was used, taking into account that the particles interacting can have different sizes and radii of influence:

$$V(r) = \begin{cases} \varepsilon\left(1 - \frac{2r}{\sigma_1+\sigma_2}\right)^{5/2} & r < \frac{\sigma_1+\sigma_2}{2} \\ 0 & r \geq \frac{\sigma_1+\sigma_2}{2}, \end{cases} \tag{4.14}$$

with σ_1 the radius of influence of particle 1 and σ_2 the radius of influence of particle 2.

In the system of Hertzian disks, only the size, and not the shape, of the particles can be changed, since the potential is spherically symmetric. Accordingly, the interaction length scale σ_i of each particle was varied sinusoidally: $\sigma_i(t) = \sigma_0 + \Delta\sigma_i \sin(\omega_i t + \phi_i)$. The reference value σ_0 is the same for all particles but the amplitude $\Delta\sigma_i$, frequency ω_i and phase ϕ_i can be different for each particle.

4.4 Results

The equation of state of Hertzian particles in two dimensions is presented in section 4.4.1, together with pictures representative of the different phases encountered upon varying the area fraction, which is a non-dimensional density and which will hereafter be referred to merely as density. For each density, 324 particles and 10^6 time steps were simulated, using the integration scheme in Eqs. 4.7 and 4.8, and the Nosé-Hoover thermostat, Eq. 4.10, with time step $\Delta t = 10^{-4}$. Temperature was set to $k_B T = 1$ and the strength of the potential to $\varepsilon = 1000$. Particles have diameter $\sigma = 1$.

For simulations of active and/or oscillating Hertzian particles, Brownian dynamics was used, according to the integration scheme in Eqs. 4.11 and 4.12. The same number of particles, time step and temperature were used. The potential strength was set to $\varepsilon = 2000$. The translational friction coefficient was set to one, $\gamma_t = 1$. Thus, the imposed translational diffusion coefficient is $D_t = D_0 = 1$. For each system, 4 simulations of $4 \cdot 10^5$ time steps were performed. The squared displacement of the particles was measured in each run and then averaged over the 4 ensembles. The curve of the mean squared displacement as a function of time was fitted to a linear function, from which the diffusion coefficient was extracted according to Eq. 4.2. All the simulations in this chapter were performed using periodic boundary conditions.

4.4.1 Passive Hertzian Particles

Simulations of Hertzian particles at different packing fractions and measurements of the virial pressure lead to the equation of state in Fig. 4.2. The change in the curve $P(\rho)$ at around $\rho \approx 1.0$ corresponds to a phase transition between a fluid phase and a triangular crystal, as is shown in Fig. 4.3.

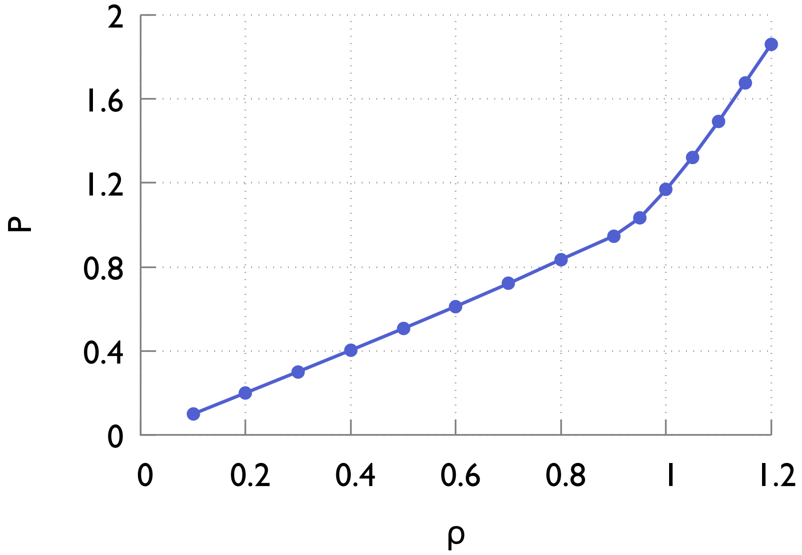

Figure 4.2: *Pressure P as a function of the packing fraction ρ of Hertzian disks in a two-dimensional box, with $\beta\epsilon = 1000$.*

The final configurations of simulations of Hertzian particles at different densities are presented in Fig. 4.3. The Fast Fourier Transform (FFT) of each phase, computed by the visualisation software of Michiel Hermes [44], is also shown. Fluid, hexagonal and squared phases are observed, as well as a dodecagonal quasicrystal phase, for which particles are arranged in pentagons and whose FFT contains 12 peaks. The only phase reported in Ref. [43] that was not observed is the stretched hexagonal phase, which would correspond to non-regular hexagons in reciprocal space. The narrowness of the range of densities for which this phase exists explains the difficulty in observing it.

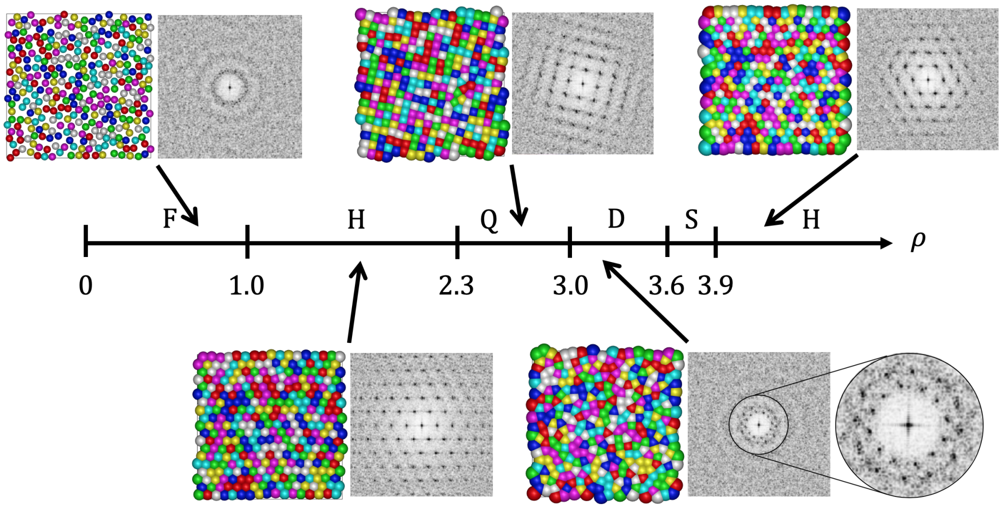

Figure 4.3: *Physical configurations and Fast Fourier Transforms of Hertzian disks at different packing fractions* ρ *for effective potential strength* $\varepsilon/k_BT = 1000$*. The numbers show the values of density, read from [43], for which phase transitions occur at this temperature. F – fluid, H – hexagonal, Q – square, D – dodecagonal quasicrystal, S – stretched hexagonal.*

4.4.2 Active Hertzian Particles

Sample plots of mean squared displacement, averaged over all particles, as a function of time are presented in Fig. 4.4. Each plot is the result of 4 simulations of a system at density $\rho = 0.1$. The plot in Fig. 4.4a shows that the mean squared displacement of passive particles ($v_0 = 0$) is linear in time, even for short time scales, in accordance with Eq. 4.2. The plot in Fig. 4.4b shows the two regimes of active partices ($v_0 = 1000$) calculated in Eq. 4.5: the quadratic, ballistic regime for short time scales and the linear, diffusive regime for long time scales. For the remainder of this chapter, we will focus on the long-term behaviour of $\langle \vec{r}^2(t) \rangle$, that is linear in time, from which the diffusion coefficient is calculated using a linear regression.

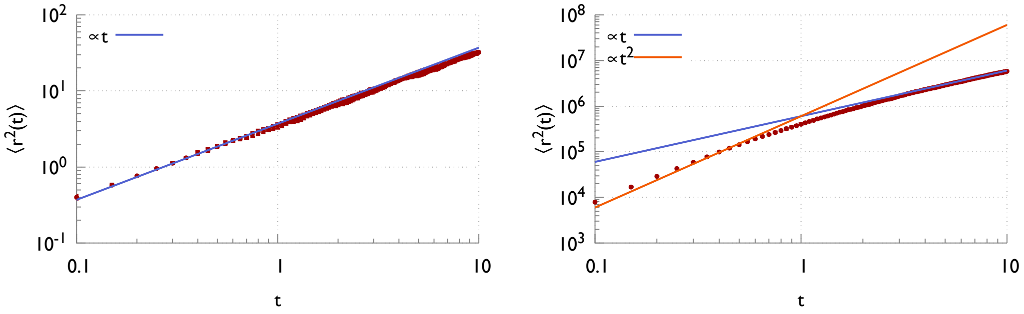

(a) *Passive,* $v_0 = 0$.

(b) *Active,* $v_0 = 1000$.

Figure 4.4: *Log plot of mean squared displacement as a function of time for a passive and an active systems at density* $\rho = 0.1$. *Only the first* 10^5 *steps are represented.*

The measured diffusion coefficients for Hertzian particles with different levels of activity are presented in Fig. 4.5, where they are compared with the analytical result for isolated active Brownian particles, $D_{\text{eff}} = D_t + v_0^2/2D_r$ (Eq. 4.6). It is clear that the diffusion coefficient increases with activity and that this increase is faster for the low density system. This is expected, since activity enhances motion, increasing the squared displacement, and low-density systems have more available space for particles to move.

Furthermore, the graph shows that low density simulations reproduce the analytical result, whereas high density simulations only do so for high values of activity, namely $v_0 = 10^4$. This is due to the fact that the analytical result is valid only for isolated particles, for which $\vec{F} = 0$. At very low densities, such as $\rho = 0.1$, this is indeed the case, since Hertzian particles barely interact. However, at very high densities, such as $\rho = 1.8$, interactions are no longer insignificant and the measured diffusion coefficient does not agree with the analytical prediction of Eq. 4.6. When the activity is sufficiently high, though, the term proportional to v_0^2 dominates over the term due to interactions and the diffusion coefficient approaches the low-density value.

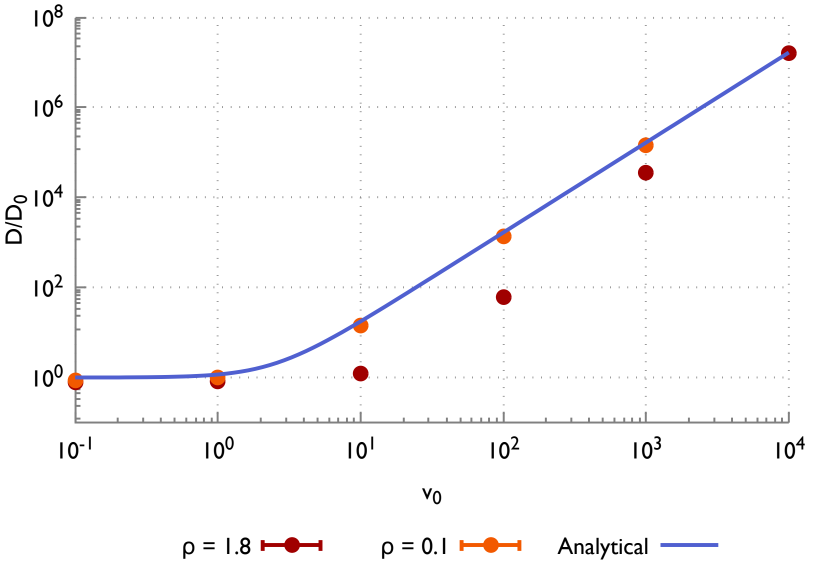

Figure 4.5: *Effective diffusion coefficient for Hertzian particles with different levels of activity* v_0 *at high and low densities, compared with analytical result* $D_{eff} = D_t + v_0^2/2D_r$. *Error bars are comparable in size to the data points.*

4.4.3 Hertzian Particles Oscillating

Simulations were performed for 6 different types of oscillation of the diameter of the particles, varying the amplitude $\Delta\sigma$ and the frequency f (see section 4.3), at 3 different densities. All particles have the same amplitude and frequency, while phases are sampled from a uniform distribution between 0 and 2π. The measured diffusion coefficients are shown in Fig. 4.6 and representative configurations at each density, with and without oscillations, are presented in Fig. 4.7.

For low densities ($\rho = 0.2$), it is visible that oscillations do not enhance movement since the diffusion coefficient is not significantly changed by the diameter variations. This happens because the amplitude of the oscillations is negligible when compared to the interparticle distance, as can be seen in a snapshot of the system in Fig. 4.7d.

For density $\rho = 1.0$, the diffusion coefficient increases when the diameter oscillates, and is higher for oscillations of larger amplitude. The fact that disks without oscillations or with very small oscillations ($\Delta\sigma = 0.1$) have nearly zero diffusion is a consequence of the system being crystallised in these cases, as can be seen in Fig. 4.7b. This triangular crystal is in accordance with the phases described in section 4.4.1, particularly Fig. 4.3. When the amplitude of the oscillations is large enough, particles are able to leave their caging positions and diffuse, leading to enhancement of motion.

For high density ($\rho = 1.8$), oscillations not only do not enhance movement, but seem to hinder the particles, since the diffusion coefficients are lower for all amplitudes. This may be due to the little available space for particles to rearrange when they collide through expansions. One could expect that the contractions would cancel out the effect of expansions but it seems that the qualitative increase in density caused by expansions dominates. Although this value of density would correspond to the triangular crystal phase, according to Fig. 4.3, the system never crystallises, even without oscillations. This is because, unlike in section 4.4.1, particles follow Brownian dynamics instead of existing in an NVT ensemble. This suggests that the friction in Brownian dynamics is much lower than that associated with a thermostat, facilitating the existence of a high-density fluid. This effect is a consequence of the softness of the potential and makes the high-density system resemble more a confluent tissue.

Finally, comparison of the results at two values of frequency, $f = 10$ and $f = 50$ (left and right columns in Fig. 4.6, respectively) shows that, in the cases where oscillations affect the diffusion coefficient ($\rho = 1.0$ and $\rho = 1.8$), the effect of higher frequencies is stronger. We can conclude that faster oscillations of greater magnitude lead to greater enhancement of motion for $\rho = 1.0$ and suppress diffusivity further in systems with $\rho = 1.8$.

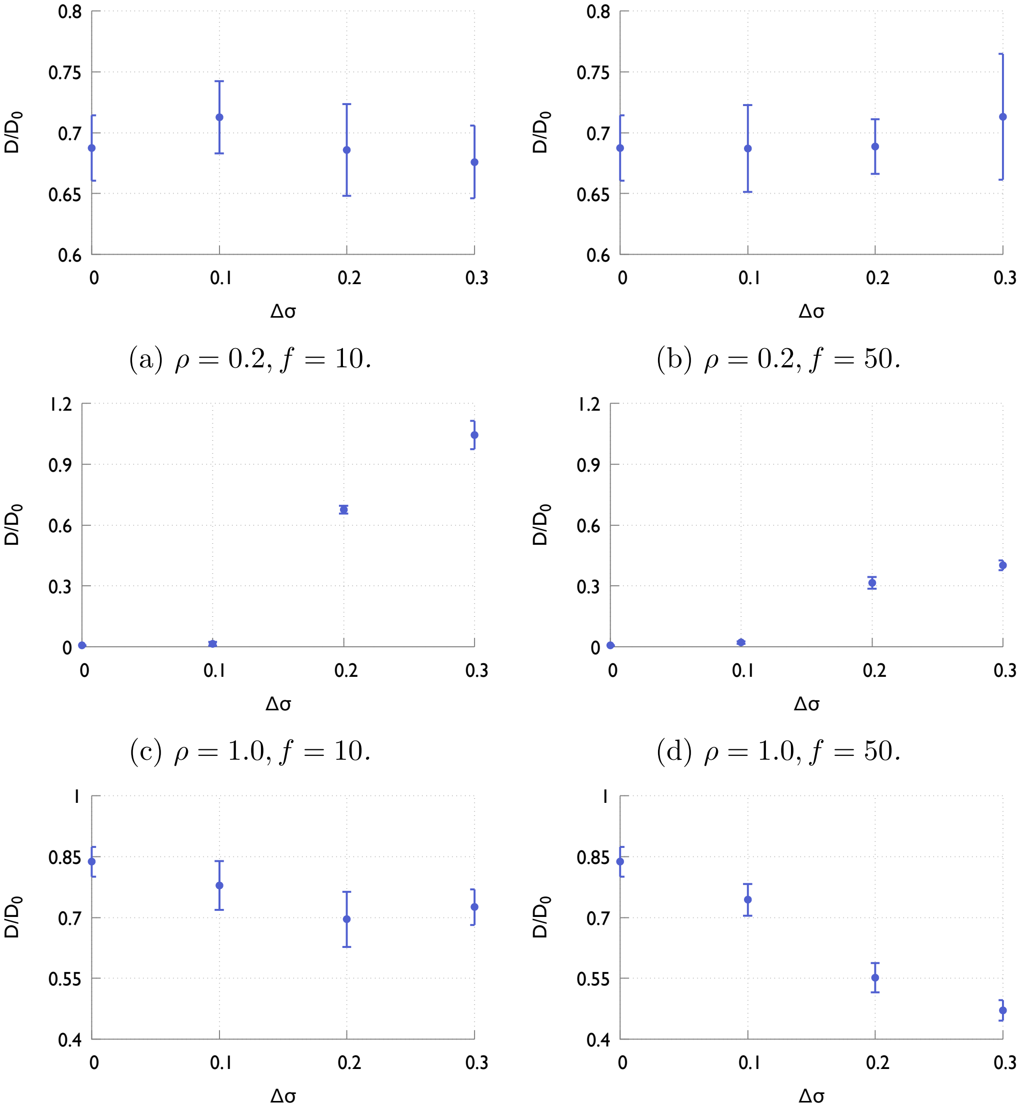

(a) $\rho = 0.2, f = 10$.

(b) $\rho = 0.2, f = 50$.

(c) $\rho = 1.0, f = 10$.

(d) $\rho = 1.0, f = 50$.

(e) $\rho = 1.8, f = 10$.

(f) $\rho = 1.8, f = 50$.

Figure 4.6: *Effective diffusion coefficient for Hertzian particles with different amplitudes of oscillating diameter* $\Delta\sigma$ *and two frequencies of oscillation* f*, at densities* $\rho = 0.2, 1.0, 1.8$*, compared with result for passive non-oscillating particles* ($\Delta\sigma = 0$)*.*

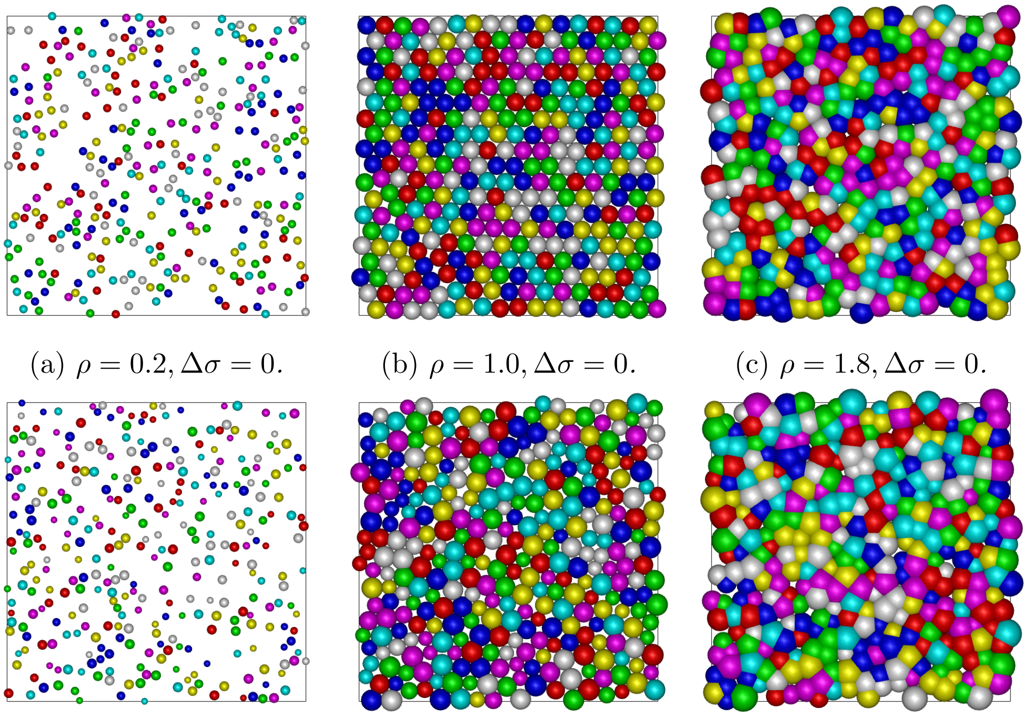

(a) $\rho = 0.2, \Delta\sigma = 0.$ (b) $\rho = 1.0, \Delta\sigma = 0.$ (c) $\rho = 1.8, \Delta\sigma = 0.$

(d) $\rho = 0.2, \Delta\sigma = 0.2.$ (e) $\rho = 1.0, \Delta\sigma = 0.2.$ (f) $\rho = 1.8, \Delta\sigma = 0.2.$

Figure 4.7: *Final configurations of the system at different densities,* $\rho = 0.2, 1.0, 1.8$*, without oscillations,* $\Delta\sigma = 0.0$*, and with oscillations of amplitude* $\Delta\sigma = 0.2$ *and frequency* $f = 10$.

4.4.4 Active Hertzian Particles Oscillating

The same types of oscillation of the previous section were simulated with activity $v_0 = 10$, to see if self-propulsion would have a non-linear effect when combined with oscillations, leading to enhancement of motion in the cases for which oscillations alone did not increase the diffusion coefficient, namely $\rho = 0.2$ and $\rho = 1.8$. The results are presented in Fig. 4.8.

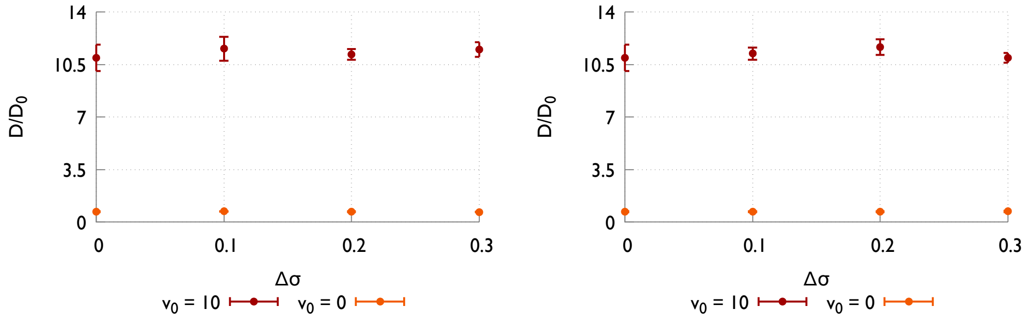

(a) $\rho = 0.2, f = 10$. (b) $\rho = 0.2, f = 50$.

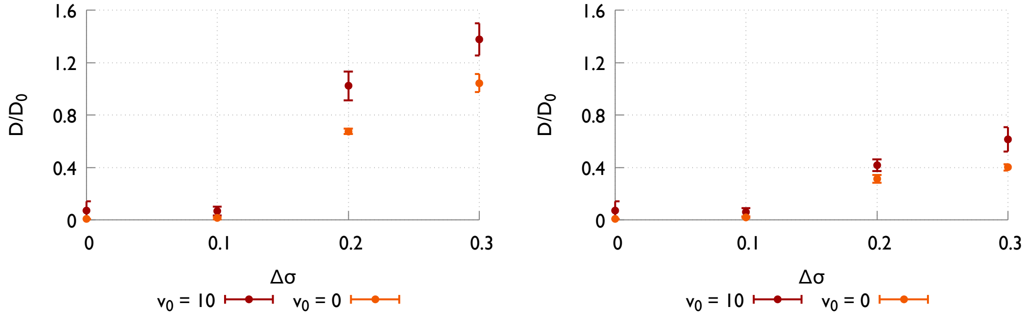

(c) $\rho = 1.0, f = 10$. (d) $\rho = 1.0, f = 50$.

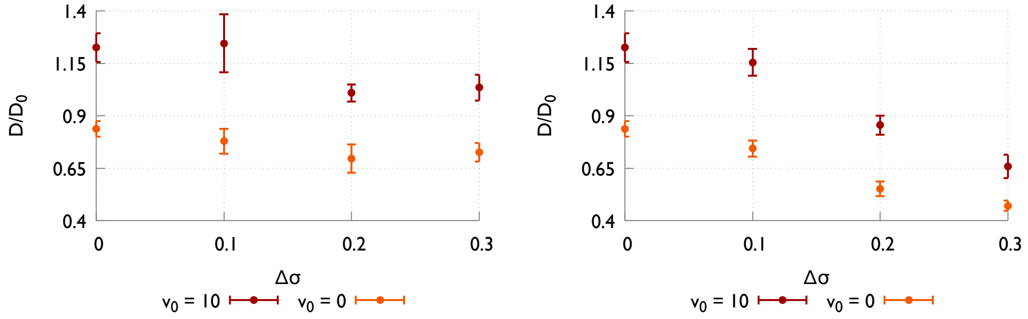

(e) $\rho = 1.8, f = 10$. (f) $\rho = 1.8, f = 50$.

Figure 4.8: *Effective diffusion coefficient for active Hertzian particles ($v_0 = 10$) with different amplitudes of oscillating diameter $\Delta\sigma$ and two frequencies of oscillation f, at densities $\rho = 0.2, 1.0, 1.8$, compared with results for passive non-oscillating particles. The diffusion coefficients of active and passive non-oscillating particles are plotted as $\Delta\sigma = 0$.*

The observed tendencies are roughly the same as those of the previous section: oscillations do not affect diffusivity for density $\rho = 0.2$, they enhance motion for $\rho = 1.0$ and they hinder motion for $\rho = 1.8$. The only difference is that the measured diffusion coefficients are shifter upwards, due to the self-propulsion. An exception to this is the cases where previously the diffusion coefficient was nearly zero ($\Delta\sigma = 0$ and $\Delta\sigma = 0.1$ at $\rho = 1.0$). Upon adding self-propulsion these systems still have nearly zero diffusivity, meaning that the level of activity is not enough to uncage the particles from the triangular crystal positions.

Chapter 5

Voronoi Model

Tests of different parts of the Voronoi implementation are presented in this chapter. First, the Voronoi diagrams and associated Delaunay triangulations of different types of cell configurations are presented and commented upon. Next, Fortune's algorithm is used to test calculation of the vertices positions using barycentric coordinates and calculation of the Voronoi diagram using the flip algorithm. Finally, a perturbed triangular lattice is used to test the time evolution calculated by the Voronoi model.

5.1 Voronoi Diagram

The implementation of Fortune's algorithm by Mathias Westerdahl [39] was adapted for configurations of seed points with periodic boundary conditions. Additionally, from the Voronoi diagram, the Delaunay triangulation was built. These computations give the expected results for a triangular lattice and for a random distribution of points, Fig. 5.1. To evaluate the accuracy of this algorithm, the maximum difference between the positions of the vertices thus calculated, $\vec{r}_{i,\text{Westerdahl}}$, and those calculated independently using Mathematica, $\vec{r}_{i,\text{Mathematica}}$, was found:

$$\text{error} = \max_i |\vec{r}_{i,\text{Westerdahl}} - \vec{r}_{i,\text{Mathematica}}| \sim 10^{-7}. \tag{5.1}$$

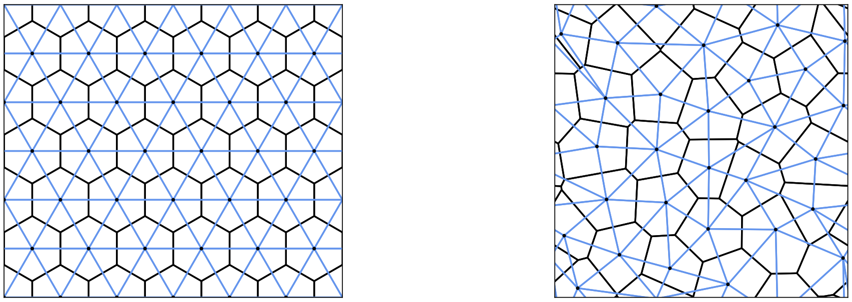

(a) *Triangular lattice.* (b) *Random configuration.*

Figure 5.1: *Voronoi diagram, in black, and Delaunay triangulation, in blue, of two different configurations of seed points, in black.*

The Voronoi diagrams of squared and hexagonal lattices can also be computed correctly, Fig. 5.2. However, these configurations are not useful for the simulation since the Delaunay triangulation for such lattices is not well defined and thus the flip algorithm cannot be used. The blue lines in Fig. 5.2 do not form triangulations, they simply represent the portions of the Delaunay triangulation that are not ambiguous. The Delaunay domains in Fig. 5.2a are actually hexagons and those in Fig. 5.2b are squares. The missing lines cannot be drawn because there are two ways of dividing each blue square in Fig. 5.2b into two triangles while respecting the Delaunay rules. Likewise, there are three ways of dividing each hexagon in Fig. 5.2a into three triangles. This a limitation of the implementation of the Voronoi model used in this project: if the tissue has even a small section with quadrangular or triangular cells, the simulation with the flip algorithm will break down.

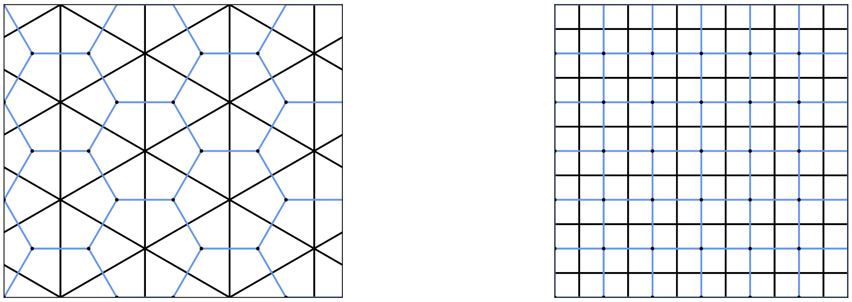

(a) *Hexagonal lattice.* (b) *Squared lattice.*

Figure 5.2: *Voronoi diagram, in black, and tentative Delaunay triangulation, in blue, of two different configurations of seed points, in black.*

Furthermore, all the vertices of a Voronoi cell are correctly associated with the site that functions as the seed of that cell. The fact that connectivity is correctly established is visible in Fig. 5.3, where gray lines connect Voronoi sites to the vertices of their polygon.

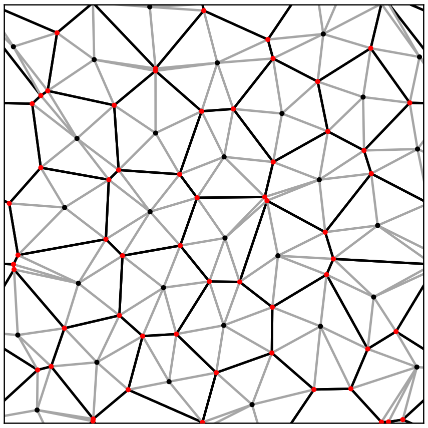

Figure 5.3: *Connectivity, represented by gray lines, between seed points, in black, and the vertices, in red, of their Voronoi polygon, in black.*

5.2 Barycentric Coordinates

The calculation of the positions of Voronoi vertices using barycentric coordinates (λ_i, λ_j, λ_k, Eq. 3.11), associated with the Delaunay triangulation, differs from those calculated using Fortune's algorithm by only $\sim 10^{-6}$, again using the error as defined in Eq. 5.1. This attests that the barycentric coordinates are well calculated in the code.

5.3 Flip Algorithm

Simulating the Voronoi model with recalculation of the diagram from scratch at every time step yields the same results as using the flip algorithm, as can be seen in Fig. 5.4. The connectivity is the same for both methods. As before, numerical comparison of the positions of the vertices showed a difference of order $\sim 10^{-6}$ between the two approaches.

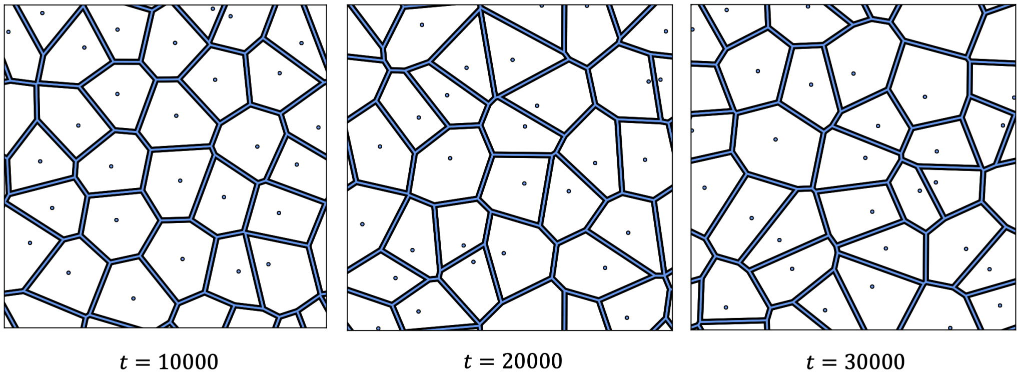

Figure 5.4: *Voronoi diagram and positions of the cell centres at 3 different instants, calculated using the flip algorithm (in black, thick lines) and Fortune's algorithm (in blue, thin lines).*

5.4 Triangular Lattice with Displaced Row

To test the validity of the integration of the Voronoi equations of motion, a triangular lattice of cell centres was first used, setting the target area and the target perimeter of all cells to the average area and perimeter. This leads to zero forces at every time step, as expected, since the lattice is perfect and all cells have the average area and perimeter. To further test the dynamics, a defect was introduced in the initial configuration by shifting one of the rows upwards, as can be seen in Fig. 5.5.

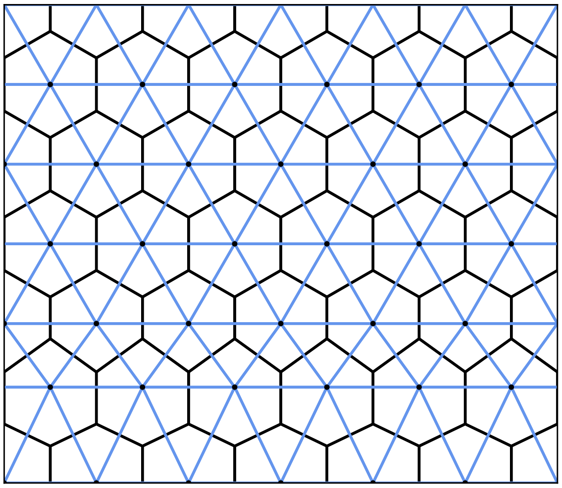

Figure 5.5: *Triangular lattice with the second row, from the bottom, displaced vertically.*

The system was studied in the absence of friction and without activity. The dynamics was found to consist of oscillations of the displaced row up and down. However, it was observed that the oscillations increase in size until the system is disrupted. Analysing the total energy as a function of time, Fig. 5.6, provides additional insights: the total energy oscillates from the beginning until it diverges at $t \approx 16$. The fact that the energy is not conserved means that something is wrong with the algorithm. Furthermore, the energy divergence and the disruption of the system are a manifestation of a significant instability.

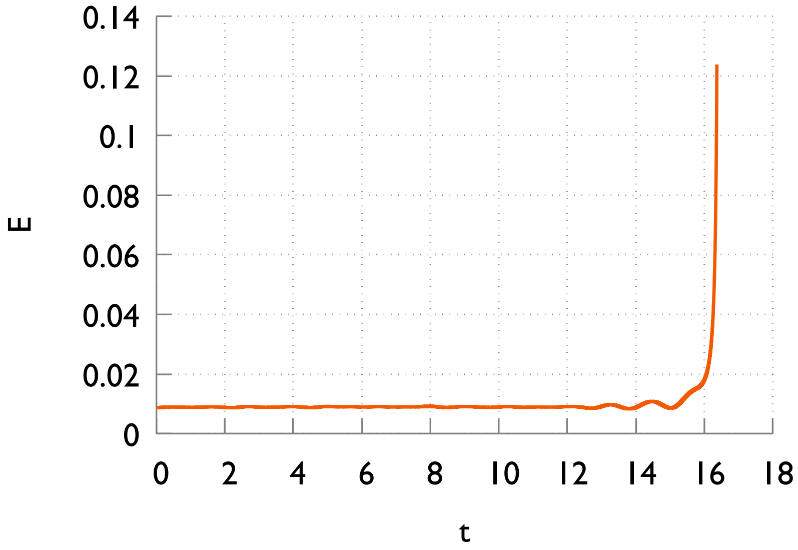

Figure 5.6: *Total energy E as a function of time t for the system shown in Fig. 5.5.*

In an attempt to find the underlying problem, an implementation of the vertex model was created (see section 3.1). The same initial configuration was used and the corresponding energy plot can be seen in Fig. 5.7. Also in this case the energy is not conserved. However, the system remains stable for a longer period of time, only diverging at $t \approx 200$. The noise-like spikes in Fig. 5.7 are in fact the result of aliasing, that is, sampling the energy at intervals that are incommensurate with the frequency of its oscillations.

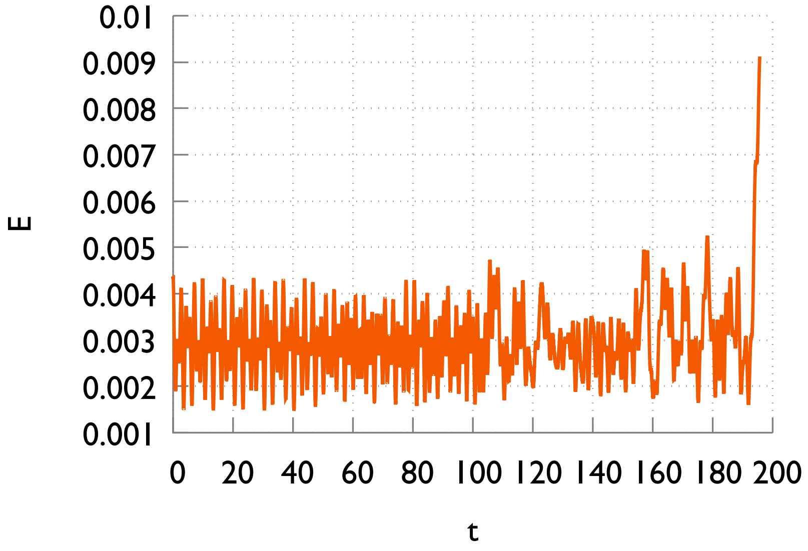

Figure 5.7: *Total energy E as a function of time t for the system shown in Fig. 5.5, using the vertex model instead of the Voronoi model.*

Chapter 6

Conclusion

Summarising, in this project two different models were implemented to study epithelial tissue and the effect of cell oscillations on collective dynamics.

The Hertz toy model employed to describe cells as particles interacting via a soft potential showed that oscillations in the size of the cells enhance motion in crystals by fluidising the system of previously caged cells. For lower densities, oscillations have no effect on the diffusion of the particles due to the significant interparticle distance and, for higher densities, which are more representative of confluent tissues, size oscillations hinder the motion of the particles.

At high density, Hertzian particles with dissipative dynamics form a fluid and not a triangular crystal, which would be expected from the phase diagram. This is due to the softness of the potential. This softness and the fact that the potential is finite at the origin raise some difficulties in the interpretation of the results, since a lot of factors such as friction and overlaps are at play. We can say conclusively that, for high densities, size oscillations hinder motion. However, several explanations are possible, from the unavailability of enough empty space for rearrangements after collisions to the increased friction associated with overlaps. The comparison with the case where enhancement is observed is further clouded by the fact that this enhancement occurs in a crystal. The caging/uncaging process is probably more significantly associated with crystal behaviour than to intrinsic features of oscillations. Further studies into the influence of oscillations using other soft potentials that do not have a phase transition near the relevant regimes could shed light on the real influence of oscillations on diffusivity.

The Voronoi model was the second model implemented and several of its features were successfully tested. Nevertheless, issues with the conservation of energy halted the intended studies with this model. Namely, shape oscillations and their influence on the fluidisation of tissues could not be accurately simulated. The underlying error in the Voronoi simulation may be a consequence of different problems.

First, it is possible that there is a minor oversight in the code. However, this was extensively checked and the fact that an implementation of the vertex model, whose calculations are much simpler, still shows non-conservation of energy suggests that a lapse is unlikely.

Another possible source of the error is the intrinsic limitations and stability problems of the Voronoi and the vertex models. The choices of parameters, namely the target areas and perimeters (or shape ratios) of the cells, can lead to divergences. Specifically, if the target area and, to a lesser extent, the target perimeter are chosen to be much larger or smaller than the average values, the system becomes overstressed or understressed, which can be aggravated by the use of periodic boundary conditions. The choice of elastic constants can also complicate matters further. Bi et al. [5] divide the area elastic constant by the perimeter elastic constant to create a non-dimensional parameter. However, this creates a problem by ruling out the possibility of ignoring the perimeter term in the equations of motion.

Therefore, although the implementation of the Voronoi model works for a number of features, further insights into the stability of the Voronoi model are needed in order to study the role of shape oscillations.

In this thesis, diffusivity was used as a measure of the fluidisation of tissues. However, other measures may be valuable to fully characterise the effect of oscillations. In addition, elastic features of tissues were not addressed. A natural starting point for this analysis is the Hertzian model. We hope the results presented here provide a solid foundation for such investigations.

Bibliography

[1] Oswald L, Grosser S, Smith DM, Käs JA. *Jamming transitions in cancer.* J. Phys. D: Appl. Phys. (2017); 50, 483001.

[2] Garcia S, Hannezo E, Elgeti J, Joanny J-F, Silberzan P, Gov NS. *Physics of active jamming during collective cellular motion in a monolayer.* Proc. Natl. Acad. Sci. U.S.A. (2015); 112(50), 15314-9.

[3] Gorfinkiel N. *From actomyosin oscillations to tissue-level deformations.* Dev. Dyn. (2015); 245(3), 268-75.

[4] Blanchard GB, Murugesu S, Adams RJ, Martinez-Arias A, Gorfinkiel N. *Cytoskeletal dynamics and supracellular organisation of cell shape fluctuations during dorsal closure.* Development (2010); 137, 2743-2752.

[5] Bi D, Yang X, Marchetti MC, Manning ML. *Motility-driven glass and jamming transitions in biological tissues.* Phys. Rev. X (2016); 6, 021011.

[6] Reece JB, Urry LA, Cain ML, Minorsky PV, Wasserman SA. *Campbell Biology* (2016, 11th ed.). New York, USA: Pearson Education.

[7] Dorland WAN. *Dorland's illustrated medical dictionary* (2012, 32nd ed.). Philadelphia, USA: Saunders/Elsevier.

[8] Dye FJ. *Dictionary of Developmental Biology and Embryology* (2011, 2nd ed.). Hoboken, USA: Wiley-Blackwell.

[9] Sinkus R, Tanter M, Xydeas T, Catheline S, Bercoff J, Fink M. *Viscoelastic shear properties of in vivo breast lesions measured by MR elastography.* Magn. Reson. Imaging (2005); 23(3), 159-65.

[10] Fritsch A, Höckel M, Kiessling T, Nnetu KD, Wietzel F, Zink M, Käs JA. *Are biomechanical changes necessary for tumour progression?* Nat. Phys. (2010); 6, 730–2.

[11] Jonietz, E. *Mechanics: the forces of cancer.* Nature (2012); 491(7425), S56–S57.

[12] Kalluri R, Weinberg RA. *The basics of epithelial-mesenchymal transition.* J. Clin. Invest. (2009); 120(5), 1786.

[13] Pittenger MF, Mackay AM, Beck SC, Jaiswal RK, Douglas R, Mosca JD, Moorman MA, Simonetti DW, Craig S, Marshak DR. *Multilineage potential of adult human mesenchymal stem cells.* Science (1999); 284(5411), 143-7.

[14] Yang J, Weinberg RA. *Epithelial-Mesenchymal Transition: At the crossroads of development and tumor metastasis.* Dev. Cell (2008); 14(6), 818-29.

[15] Morel A-P, Lièvre M, Thomas C, Hinkal G, Ansieau S, Puisieux A. *Generation of breast cancer stem cells through epithelial-mesenchymal transition.* PLoS One (2008); 3(8), e2888.

[16] Stone RC, Pastar I, Ojeh N, Chen V, Liu S, Garzon KI, Tomic-Canic M. *Epithelial-mesenchymal transition in tissue repair and fibrosis.* Cell Tissue Res. (2016); 365(3), 495-506.

[17] Fuxea J, Karlssonb MCI. *TGF-β-induced epithelial-mesenchymal transition: A link between cancer and inflammation.* Sem. Cancer Biol. (2012); 22(5-6), 455-61.

[18] Pawlizak S, Fritsch AW, Grosser S, Ahrens D, Thalheim T, Riedel S, Kießler TR, Oswald L, Zink M, Manning ML. *Testing the differential adhesion hypothesis across the epithelial-mesenchymal transition.* New J. Phys. (2015); 17, 083049.

[19] Schötz E-M, Lanio M, Talbot JA, Manning ML. *Glassy dynamics in three-dimensional embryonic tissues.* J. R. Soc. Interface (2013); 10, 20130726.

[20] Camley BA, Rappel W-J. *Physical models of collective cell motility: from cell to tissue.* J. Phys. D: Appl. Phys. (2017); 50(11), 113002.

[21] Palsson E, Othmer HG. *A model for individual and collective cell movement in Dictyostelium discoideum.* Proc. Natl. Acad. Sci. U.S.A. (2000); 97(19), 10448-10453.

[22] Coburn L, Cerone L, Torney C, Couzin ID, Neufeld Z. *Tactile interactions lead to coherent motion and enhanced chemotaxis of migrating cells.* Phys. Biol. (2013); 10(4), 046002.

[23] Nematbakhsh A, Sun W, Brodskiy PA, Amiri A, Narciso C, Xu Z, Zartman JJ, Alber M. *Multi-scale computational study of the mechanical regulation of cell mitotic rounding in epithelia.* PLoS Comput. Biol. (2017); 13, e1005533.

[24] Szabó A, Unnep R, Méhes E, Twal WO, Argraves WS, Cao Y, Czirók A. *Collective cell motion in endothelial monolayers.* Phys. Biol. (2010); 7(4), 046007.

[25] Nagai T, Honda H. *A dynamic cell model for the formation of epithelial tissues.* Philos. Mag. B (2001); 81(7), 699-719.

[26] Nonomura M. *Study on multicellular systems using a phase field model.* PLoS One (2012); 7(4), e33501.

[27] Lee P, Wolgemuth CW. *Crawling cells can close wounds without purse strings or signalling.* PLoS Comput. Biol. (2011); 7(3), e1002007.

[28] Vig DK, Hamby AE, Wolgemuth CW. *Cellular contraction can drive rapid epithelial flows.* Biophys. J. (2017); 113, 1613–1622.

[29] Curran S, Strandkvist C, Bathmann J, de Gennes M, Kabla A, Salbreux G, Baum B. *Myosin II controls junction fluctuations to guide epithelial tissue ordering.* Dev. Cell (2017); 43(4), 480-492.

[30] Barton DL, Henkes S, Weijer CJ, Sknepnek R. *Active Vertex Model for cell-resolution description of epithelial tissue mechanics.* PLoS Comput. Biol. (2017); 13(6), e1005569.

[31] Hiraiwa T, Wen F-L, Shibata T, Kuranaga E. *Mathematical modeling of tissue folding and asymmetric tissue flow during epithelial morphogenesis*. Symmetry (2019); 11, 113.

[32] Liu AJ, Nagel SR. *The jamming transition and the marginally jammed solid*. Annu. Rev. Condens. Matter Phys. (2010); 1, 347–69.

[33] Gibbs JH, DiMarzio EA. *Nature of the glass transition and the glassy state*. J. Chem. Phys. (1958); 28, 373.

[34] Teomy E, Kessler DA, Levine H. *Confluent and nonconfluent phases in a model of cell tissue*. Phys. Rev. E (2018); 98, 042418.

[35] Paluch E, Piel M, Prost J, Bornens M, Sykes C. *Cortical actomyosin breakage triggers shape oscillations in cells and cell fragments*. Biophys. J. (2005); 89(1), 724-733.

[36] Hiraiwa T, Kuranaga E, Shibata T. *Wave propagation of junctional remodeling in collective cell movement of epithelial tissue: numerical simulation study*. Cell Dev. Biol. (2017); 5, 66.

[37] Sadeghipour E, Garcia MA, Nelson WJ, Pruitt BL. *Shear-induced damped oscillations in an epithelium depend on actomyosin contraction and E-cadherin cell adhesion*. eLife (2018); 7, e39640.

[38] Heunis J. *Fortune's algorithm: an intuitive explanation* [Web log post]. March 2018. Retrieved April 2019 from https://github.com

[39] Westerdahl M. *A C implementation for creating 2D Voronoi diagrams*. March 2015. Retrieved February 2019 from https://github.com

[40] Frenkel D, Smit B. *Understanding molecular simulation: from algorithms to applications* (2001, 2nd ed.). Cambridge, USA: Academic Press.

[41] Winkler RG, Wysocki A, Gompper G. *Virial pressure in systems of spherical active Brownian particles*. Soft Matter (2015); 11, 6680-6691.

[42] Howse JR, Jones RAL, Ryan AJ, Gough T, Vafabakhsh R, Golestanian R. *Self-motile colloidal particles: from directed propulsion to random walk*. Phys. Rev. Lett. (2007); 99(4), 048102.

[43] Pàmies JC, Cacciuto A, Frenkel D. *Phase diagram of Hertzian spheres.* J. Chem. Phys. (2009); 131, 159903.

[44] Hermes M. *Visualizing colloids* [Online software]. 2012. Retrieved June 2019 from https://michielhermes.github.io/viscol/viewer/index.html

Acknowledgements

First and foremost, I would like to thank my supervisor Joost de Graaf for all the guidance, help and support throughout this project. Thank you for the discussions, for always being willing to answer my questions and for being in the trenches with me when the code did not cooperate. I am also grateful for your thoughtful suggestions and keen eye as editor of this manuscript.

I would also like to acknowledge the friends that coloured my life in Utrecht and made me feel more at home, and those that, even far away, always lent me a helping hand and were with me in this journey.

Finally, I want to thank, though clumsily because words fail me, the unconditional love and support of my parents, sister and boyfriend. You are my pillars, my magic and my happiness. Obrigada por tudo.